EFFECTS OF SECONDARY ELECTRON EMISSION ON THE COLLECTOR AND SOURCE SHEATHS OF A FINITE ION TEMPERATURE PLASMA

by

L. A. Schwager

Memorandum No. UCB/ERL M88/24

13 April 1988

EFFECTS OF SECONDARY ELECTRON EMISSION ON THE COLLECTOR AND SOURCE SHEATHS OF A FINITE ION TEMPERATURE PLASMA

by

L. A. Schwager

Memorandum No. UCB/ERL M88/24

13 April 1988

ELECTRONICS RESEARCH LABORATORY

College of Engineering
University of California, Berkeley
94720

EFFECTS OF SECONDARY ELECTRON EMISSION ON THE COLLECTOR AND SOURCE SHEATHS OF A FINITE ION TEMPERATURE PLASMA

by

L. A. Schwager

Memorandum No. UCB/ERL M88/24

13 April 1988

ELECTRONICS RESEARCH LABORATORY

College of Engineering
University of California, Berkeley
94720

Table of Contents

2

Effects of Secondary Electron Emission on the Collector and Source Sheaths of a Finite Ion Temperature Plasma

The region between a Maxwellian plasma source and an absorbing surface which emits cool secondary electrons is modeled numerically with dynamic, electrostatic particle simulation and theoretically with a static, kinetic plasma-sheath model. The coefficient of secondary electron emission is varied up to and beyond critical emission which causes electric field reversal at the collector. Results from these models agree very well over this wide range of emission coefficients. Increasing the secondary emission coefficient reduces the collector potential which increases the total energy flux to the collector while decreasing the ion energy deposited. In the simulation, some heating of the secondary electron stream is observed to gradually evolve over many Debye lengths, possibly because of a beam-plasma interaction. This heating increases potential fluctuations but causes only small deviations from the predictions with static theory.

I. INTRODUCTION

A. Problem Description

Near an electrically floating collector, an electrostatic sheath forms which impedes the flow of plasma electrons in order to balance ion and electron currents at the collector surface. For plasma temperatures of 10–1000 eV and many types of collector materials, an electron striking the surface either can be elastically scattered or, more often, can cause the ejection of one or more secondary electrons.[1] Generally these electrons eject from the valence band of the material with a temperature of a few electron volts. This secondary electron emission reduces substantially the potential drop across the collector sheath. At the collector, this reduced potential decreases the incident ion energy, which lowers the sputtering of material,[2] while increasing the total energy flux deposited. In addition, the interaction between the cool secondary electron stream and the warmer ambient plasma enhances potential fluctuations and heats the electron stream.

The sheath region near an emissive surface is rich in kinetic behavior, having non-Maxwellian velocity distributions of the source ions and electrons and the cooler secondary electrons. Time-dependent computer simulations using the particle-in-cell method are a prime tool for examining these non-neutral plasma regions and following the dynamics of the plasma-sheath-surface interaction. These simulations can provide insight for verifying and improving the kinetic model for the steady state conditions. Consequently, kinetic theory and simulation are both developed to analyze this region and are found in excellent agreement.

The conceptual evolution from the fully bounded plasma to the present theoretical and simulation model of the sheath region is shown in Fig. 1. In a plasma device, the source of Maxwellian ions and electrons is distributed across a region several orders of magnitude larger than a plasma Debye length λ_D. As described

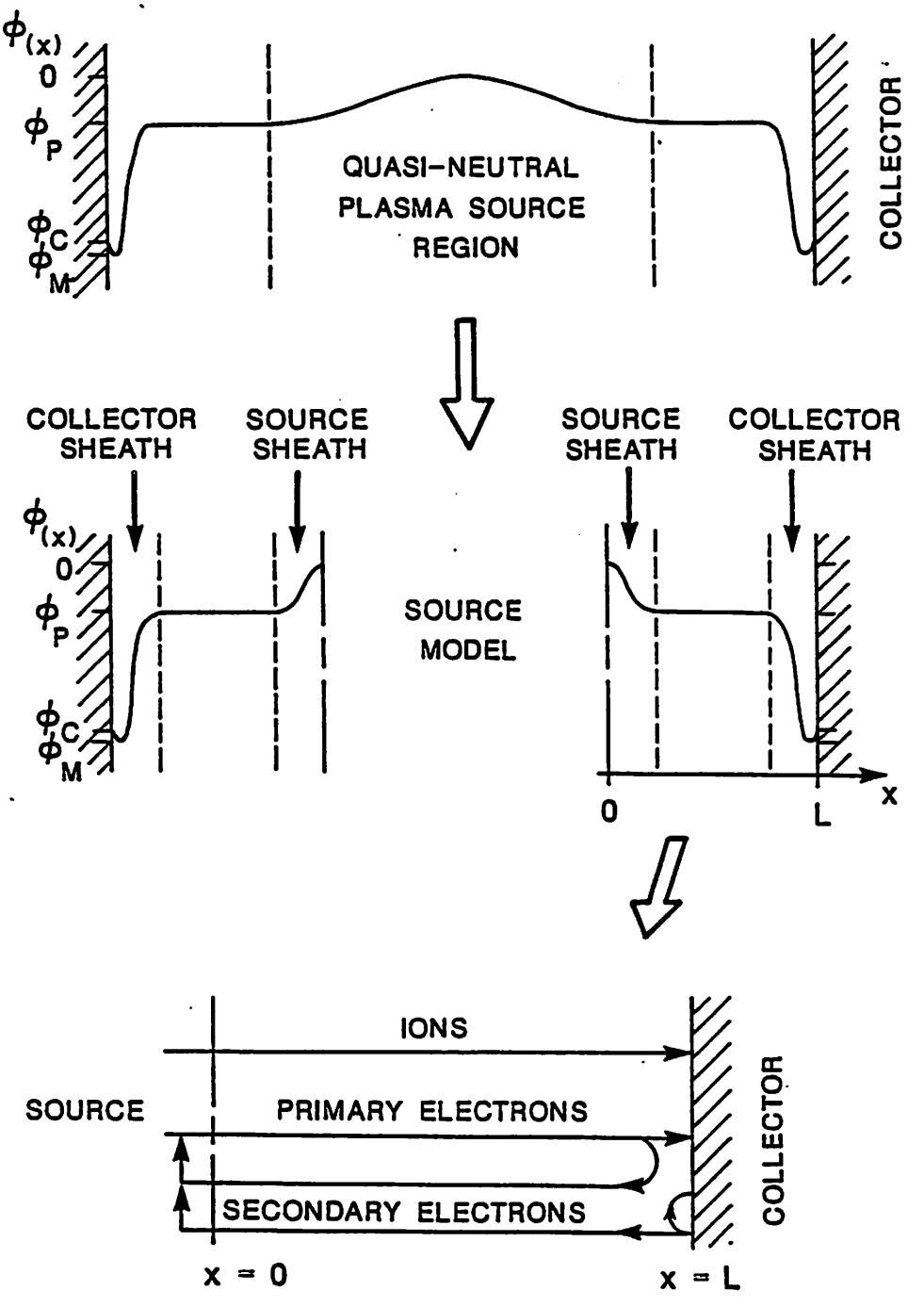

FIG. 1. Model and form of the electrostatic potential profile for the non-Maxwellian sheath region between a Maxwellian plasma source and an electrically floating collector that emits secondary electrons. The top figure indicates the form of the potential profile for a distributed source. The source region is many orders of magnitude longer than the collector sheath region. The middle shows the potential profile expected for a planar source. The bottom diagrams the flow of particles between the source plane and collector.

by Emmert[4] and shown in the first potential profile in Fig. 1, the electrostatic potential falls to ϕ_P over the source region and then falls again to ϕ_C through the collector sheath. In my model shown in the second profile, the plasma source exists entirely within the plane at $x=0$. Hence the potential drop through the source region occurs fully within a few λ_D from the source itself; this "source sheath" is observed via simulation and described in the previous paper.[3] In this way the effects of secondary electron emission on the source sheath as well as the collector sheath are analyzed.

The plasma source emits steady and equal fluxes of ions and electrons, each with half-Maxwellian velocity distributions. The temperature and mass ratios of these ions and electrons are specified. As these particles flow to an electrically floating plate (at potential ϕ_C), it becomes charged by the incident particles. This collector plate emits a flux of secondary electrons, F_2, which depends on the incident primary electron flux F_e according to the secondary electron emission coefficient $\gamma = -F_2/F_e$. This coefficient is independent of the energy of incident primary electrons. However, incident secondary electrons which may have been repelled by the collector sheath back to the collector are not allowed to generate more secondaries. The collector emits secondary electrons with a half-Maxwellian velocity distribution at a temperature T_{C2} which is one percent of the electron source temperature T_{Se}. (Throughout this paper, temperature measured in energy units.)

Particles which return to the plasma source are added to the steady flux injected at the source temperature. These particles have been either repelled by the internal electrostatic field or emitted by the collector and accelerated by the field. Sketched at the bottom of Fig. 1, this "refluxing" at the source prevents any charge accumulation at the source plane which enforces a zero electric field at the plasma boundary. Reaching the source region, the secondary electrons are assumed to in-

teract with the source particles so that they also reflux with the electron source temperature. The possible effect of the secondaries reducing the electron source temperature plasma beyond the sheath region is not included in my model.

For primary electrons, the effective source density (and flux) emitted into the region increases beyond the source density injected initially. After a time, this increase occurs because secondary electrons and repelled primary electrons arrive at the source and are refluxed. Hence, in steady state, the magnitude of the velocity distribution for primary electrons is not fixed but is determined by γ and ϕ_C self-consistently (to be shown in Sec. II C 2).

The preceeding conditions are intended to model the source and collector sheath regions of a symmetric, bounded plasma with a central, full-Maxwellian source region. The region between the plasma source and collector is treated as collisionless; the source itself is implied collisional. These assumptions and boundary conditions, with the exception of the secondary electron emission at the collector, are identical to those given in a previous paper which analyzes the sheath region near a purely absorbing collector.[3]

The source and collector sheaths, sketched in the middle of Fig. 1, serve, respectively, to neutralize the incoming source plasma and to maintain a zero net current at the collector. The potential drop across the source sheath, ϕ_P, becomes more negative primarily when the ion/electron source temperature ratio, $\tau = T_{Si}/T_{Se}$, is decreased. The potential drop across the collector sheath, $\phi_C - \phi_P$, becomes more negative primarily when the electron/ion mass ratio, $\mu = m/M$, is increased. For a D-T plasma (with a mean value of $\mu = 1/4590$) and $\tau = 1$, the presence of a strongly emissive collector increases the electron density in the system. This increase causes a more positive potential curvature, $\nabla^2\phi$, overall which raises $e\phi_C$ from $-3T_{Se}$ to $-1\,T_{Se}$. (The unsigned charge e is equal for all three species.) In addition, for $\tau = 1$

and $\mu \ll 1$, then $e\phi_P = -0.34 T_{Se}$. Thus ϕ_P comprises significantly one-third of the total potential drop. For $\gamma = 0$, a detailed discussion of the source and collector sheath evolution along with the derivation of the dependence of ϕ_P and ϕ_C on μ and τ is provided in a previous paper.[3]

A minimum potential ϕ_M, shown in the collector sheaths sketched in Fig. 1, evolves when γ is increased beyond the critical emission coefficient, defined as γ_c, which causes electric field reversal at the collector. This occurs because the low energy secondary electrons reduce the space charge in front of the collector. For secondary emission beyond γ_c, the electric field becomes more negative and a potential minimum ϕ_M appears below ϕ_C; the potential profile is no longer monotonically decreasing. The potential dip, $\Delta\phi = \phi_C - \phi_M$, adjusts to allow no more secondary current than that which occurs when the collector emission coefficient equals γ_c in steady state. Only secondary electrons emitted with an energy greater than $e\Delta\phi$ will pass beyond the collector sheath toward the plasma source. Consequently $\phi_C - \phi_M$ depends on the ratio of γ to γ_c and the temperature ratio of the secondary to primary electrons, $\sigma = T_{C2}/T_{Se}$. Defined as the coefficient causing a zero collector field, γ_c is a function of only μ and τ.

The bounded, electrostatic simulation utilizes the particle-in-cell method for one dimension in space x and velocity v. The time-evolution of the initially empty system is monitored until a steady-state configuration is achieved. The transient response and plasma oscillations of the collective behavior are measured. Because the simulation generates the velocity distribution of the ions and electrons in space and time, the spatial profiles and temporal histories of various energy and particle fluxes are calculated.

The kinetic theory models the steady state configuration of the region and satisfies Poisson's equation and Vlasov equations applied to a potential profile which

decreases monotonically from the source to the collector. The full kinetic description of the ions and both types of electrons determines the exact dependence of all three densities on the potential profile. Then with this description, various energy and particle fluxes are derived as a function of potential at any spatial location.

For both the theory and simulation, the boundary conditions of a zero electric field at the source and zero total current at the collector, with a fixed secondary emission coefficient γ, are applied as above. The electric field is assumed to be zero at the inflection point in potential which occurs in the central region sufficiently separating the source and collector sheaths by many Debye lengths. Recall also that the magnitude of the velocity distribution of primary electrons emitted at $x = 0$ is dependent on ϕ_C because of refluxing. With Poisson's equation and the above assumptions and conditions, the values of potential at the neutral region, ϕ_P (also defined as the source sheath drop), and at the collector, ϕ_C, are calculated as a function of mass and temperature ratios and emission coefficient. For $\gamma = \gamma_c$, the added boundary condition of zero field at the collector determines the dependence of γ_c on μ, τ, and σ. These results are also valid for $\gamma > \gamma_c$ provided that $\sigma \ll 1$ which assures that $\phi_M \approx \phi_C$.

Details of the above kinetic theory are provided in Sec. II. The numerical simulation model and results are compared to the kinetic theory and presented in Sec. III. In Sec. IV is a detailed description of how this kinetic model differs from previous sheath studies which are summarized below. Conclusions are given in Sec. V.

B. Historical Review

A general comparison of the assumptions of various authors[2,5–10] is presented in Table I. The analysis of Hobbs and Wesson[5] provides a simple method of finding

TABLE I. Comparison of assumptions by various authors on the analysis of secondary electron emission effects on the sheath region. The term "Boltzmann" refers to an $\exp(\phi)$ density dependence and "cut-off" refers to the accounting of minimum energy as a function of ψ which causes an $\mathrm{erf}(\phi)$ density dependence. The parameter E_M is the minimum ion energy at the collector sheath edge. The parameter f_{C2} is the energy distribution of emitted electrons. Temperature ratios $\tau = T_{Si}/T_{Se}$ and $\sigma = T_{C2}/T_{Se}$.

Authors	Primary Electrons	Secondary Electrons	Ions
Hobbs and Wesson[5]	Boltzmann	$\sigma \ll 1$	$\tau \ll 1$ E_M derived
Stangeby[6]	Boltzmann	$\sigma \ll 1$	variable τ E_M assumed
Nicolai and Fuchs[2,a]	Boltzmann	variable σ Boltzmann	variable τ Boltzmann
Harbour[7]	cut-off	$\sigma \ll 1$	E_M varied
Hall and Bernstein[8]	cut-off	variable σ cut-off	$\tau \ll 1$ E_M derived
Sizonenko[9]	cut-off	variable f_{C2} cut-off	$\tau \ll 1$ E_M derived
Brooks[10,b]	cut-off	variable σ cut-off	variable τ E_M varied
Schwager	cut-off	variable σ cut-off	variable τ cut-off

[a] Use a transport code which includes sputtering; no analytic expression is derived.

[b] Uses a kinetic Vlasov code which includes sputtering; no analytic expression is derived.

the potential at the electrically floating collector as a function of μ and γ. They model the electron density with a Boltzmann factor and the ions and secondary electrons as a cold beam. The plasma source, infinitely far from the collector, is assumed to have zero potential and zero field. Cold ions arrive at the sheath edge with a minimum energy E_M, which is determined by integrating Poisson's equation once and using the above conditions at the source. They derive a Bohm criterion[11] which is modified for secondary electron emission. The potential which accelerates the cold ions to E_M is assumed to be negligible and so is not self-consistently included in the full potential change from the plasma source to the collector. For the case of zero field at the collector, they determine the dependence of γ_c on μ.

Subsequent authors have modeled the ions and electrons more exactly with various combinations of assumptions, listed in Table I. Those who include the minimum or cut-off particle energy (dependent on ϕ according to energy conservation), in the evaluation of Poisson's equation are the closest to first principles. This approach produces densities having the form of erf(ϕ). Allowing the cut-off energy to become very large results in a Boltzmann factor density dependence. The use of Boltzmann factors for densities within the sheath, at least in the case of a purely absorbing collector, overpredicts electron densities by a factor of two as $\phi \rightarrow \phi_C$, as discussed in the previous paper.[3]

Evaluations of the minimum ion energy at the collector sheath edge, E_M, differ for each of the authors listed in Table I. Hall and Bernstein[8] and Sizonenko[9] evaluate E_M by deriving a "modified Bohm criterion", as did Hobbs and Wesson, with the zero potential and field conditions far from the collector. Harbour[7] and Brooks[10] use E_M as a variable parameter which must exceed the Bohm solution of $T_{Se}/2$. Stangeby[6] assumes that (independent of γ) $E_M = (T_{Se} + T_{Si})/2$, where T_{Si} is the ion temperature in the source. All of these approaches result in a different expression

for ϕ_C.

The method used in the present paper of modeling the plasma members with truncated velocity distributions is the same as that used in the previous paper[3] and by Kuhn[12] and others referenced in the previous paper. In particular, McIntyre[13] models electron emission from the cold anode of a thermionic convertor. The nature of the thermionic convertor allows a bias applied across the hot emitter and cold collector and a fixed ratio α of the ion to electron density emitted at the hot cathode. In my model, the plasma source is not at an emissive surface which collects charge. Hence, the neutralization parameter α is not fixed but will vary with the floating collector potential ϕ_C. (This expression will be derived in Sec. II C 2.) The dependence of the ion and primary and secondary electron densities on the potential profile is the same as that derived by McIntyre. We differ in the assumption of zero field and the dependence of α on ϕ_C.

Only the present author determines the dependence of γ_c on μ and τ. Allowing the secondary electrons to have a finite temperature is the only way $\gamma_c(\mu, \tau)$ can be evaluated otherwise the secondary electron density goes to infinity at the collector when the zero field condition at the collector is applied. Nevertheless, from the expressions of Hobbs and Wesson, $\gamma_c(\mu)$ can be plotted for $\tau \ll 1$, which agrees closely with my results for $\mu < 0.005$ at $\tau \leq 1$.

II. THEORY

A. Model and assumptions

The source and collector sheaths characterizing a bounded, symmetric plasma, as shown in the middle of Fig. 1, is modeled over the distance from $x > 0$ to the collector at $x = L$. A plasma source at the reference potential, at $x = 0$, injects

temporally constant, equal fluxes of ions and electrons, each with a half-Maxwellian distribution of velocity. The ratio of electron to ion mass, $\mu = m/M$, is a fixed parameter as well as the ratio of ion to electron source temperature, $\tau = T_{Si}/T_{Se}$. The electric field is zero at $x = 0$ because of refluxing which allows no surface charge to exist there.

At $x = L$, the collector electrically floats to ϕ_C, absorbs and is charged by all incident particles, and emits electron-induced secondary electrons which increases the collector charge. The collector emits these secondaries with a half-Maxwellian distribution of velocity at temperature $T_{C2} = \sigma T_{Se}$. The emitted current F_2 equals $-\gamma F_e$ which for this steady state analysis is temporally constant. The emission coefficient γ and secondary temperature ratio σ are fixed parameters. Net electrical current at the collector is zero as the collector is not electrically connected to the external world. When $\gamma = \gamma_c$, the electric field equals zero at $\phi = \phi_C$ by definition.

The value of potential is designated ϕ_P at the neutral or inflection point, where $\nabla^2\phi = 0$, between the source and collector sheaths. The electric field $-\nabla\phi$ at ϕ_P, which by definition is a constant, is chosen to be zero, when the source and collector sheaths are many Debye lengths apart.

B. Derivation of velocity distributions

The velocity distributions are governed by conservation of energy as shown in the previous paper.[3] The electrostatic potential is assumed to be monotonically decreasing with position (for $\gamma < \gamma_c$). Consequently, the velocity distribution of the ions is an accelerated half-Maxwellian; all ions reach the collector. The source and collector potential drops repel most of the electrons; only the fastest electrons reach the collector. Hence, the electron velocity distribution is a truncated, decelerated full-Maxwellian. The velocity distribution of secondary electrons (for $\gamma \leq \gamma_c$) is

an accelerated half-Maxwellian; all secondaries reach the source at $x = 0$. As a result, the minimum velocity, $-V_{M2}$, (that of the slowest secondary electron) can be expressed using conservation of energy as

$$-V_{M2}(x) = \left[\frac{2}{m}(e\phi(x) - e\phi_C)\right]^{1/2}$$

where m is electron mass. Thus the velocity distribution of the secondary electrons, f_2, for any potential value is

$$f_2(\psi, v) = N_{C2}\left(\frac{m}{2\pi\sigma T_{Se}}\right)^{1/2} \exp\left(\frac{\psi - \psi_C}{\sigma} - \beta_2 v^2\right)\Theta(V_{M2}(\psi) - v) \qquad (1)$$

where v is particle velocity; N_{C2} is the secondary electron density of the full-Maxwellian source within the collector ($x > L$); ψ is normalized potential $e\phi/T_{Se}$; β_2 is $m/(2\sigma T_{Se})$; and Θ is the Heaviside step function. The derivations for ion and primary electron values of minimum velocity and velocity distributions are presented in the previous paper[3] and are valid here. Hence, for any value of potential, the distribution function for each species (ions and primary and secondary electrons) in the collisionless sheath region is known.

C. Derivation of moments

1. *Definitions*

Determining the various moments for each species of particles using the distribution functions in Eq. (1) and in Eqs. (1) and (2) of the previous paper[3] provides the potential dependence for each moment. The general definitions which use the velocity moments to evaluate density N, particle flux F, drift velocity $\langle V \rangle$, temperature T, kinetic energy flux Q, and heat flux H are presented in Sec. II C 1, also in the previous paper. The examples shown are for the ions but the same expressions within each integral apply for primary and secondary electrons. For the secondary

electrons, the lower limit of integration is $v = -\infty$ and the upper is $V_{M2}(\psi)$ (also negative). Terms for ions and primary and secondary electrons will be denoted with subscripts i, e, and 2, respectively.

2. *Secondary electron density and electron fluxes*

An evaluation of the first velocity moments for all three species shows that F_i, F_e, and F_2, are spatially constant. With no creation or annihilation of particles along $0 < x < L$ and when the loss rate of particles equals the injection rate then, $\partial N/\partial t = 0$ so that $\nabla \cdot \mathbf{F} = 0$, by conservation of particles. Thus in my one-dimensional system at steady state, $\mathbf{F}$ is spatially constant for each species.

The net particle fluxes emitted from the source are assumed to be temporally constant. The condition of zero collector current and the definition of γ determines the flux balance at the collector. Thus both electron fluxes, normalized to $F_i(\psi) = F$, are expressed as

$$F_e = F/(1-\gamma) \tag{2}$$

and

$$F_2 = -\gamma F/(1-\gamma). \tag{3}$$

Evaluating F_2 over all velocities for the secondary electrons gives

$$F_2 = -N_{C2}\left(\frac{\sigma T_{Se}}{2\pi m}\right)^{1/2}. \tag{4}$$

The electron flux F_e has the same dependence on $\exp \psi_C$ and N_{Se} as expressed in Eq. (10) of the previous paper.[3]

The neutralization parameter α for my system is evaluated with these flux expressions. This evaluation is in keeping with the traditional description used by previous authors[11,12] to describe the hot emitting cathode of a thermionic emitter

or Q-machine. Combining Eq. (2) with Eqs. (9) and (10) of the previous paper determines that the ratio α of emission densities is

$$N_{Si}/N_{Se} = (1-\gamma)(\mu\tau)^{-1/2}\exp(\psi_C).$$

The ion source density is proportional to the fixed ion flux F from Eq. (9) of the previous paper. Thus, the primary electron source effectively emits a density which depends on γ and ψ_C.

Substituting Eqs. (3) and (4) into the integral of Eq. (1) expressed in terms of F yields the secondary electron density:

$$N_2(\psi) = \frac{\gamma F}{1-\gamma}\left(\frac{\pi m}{2\sigma T_{Se}}\right)^{1/2}\exp\left(\frac{\psi-\psi_C}{\sigma}\right)\mathrm{erfc}\left(\frac{\psi-\psi_C}{\sigma}\right)^{1/2}. \qquad (5)$$

The density expressions in Eqs. (11) and (12) for $N_i(\psi)$ and $N_e(\psi)$ of the previous work also apply here if the the F term in Eq. (12) for the primary electrons is replaced with $F/(1-\gamma)$.

If the secondaries are emitted with zero temperature and zero drift velocity, then, using energy conservation and Eq. (4), the density of this cold beam can be expressed simply as

$$N_2(\psi) = \frac{\gamma F}{1-\gamma}\left(\frac{\pi m}{4\sigma T_{Se}}\right)^{1/2}(\psi-\psi_C)^{-1/2}.$$

This expression is questionable at the collector where $N_2 \to \infty$ and $\langle V_2\rangle \to 0$ but the product $N_2\langle V_2\rangle$ is constant.

3. *Secondary electron temperature and energy fluxes*

With the collisionless sheath model, temperature is effectively defined as the mean square deviation of velocity about the mean. With this definition, the dependence of secondary electron temperature on potential becomes

$$\frac{T_2(\psi)}{\sigma T_{Se}} = \frac{1-(2/\pi)^{1/2}m^{3/2}(\sigma T_{Se})^{-3/2}G(\beta_2, V_{M2}(\psi))}{\mathrm{erfc}\left[(\psi-\psi_C)/\sigma\right]^{1/2}}$$

$$- \frac{2\exp\left[(2\psi_C - 2\psi)/\sigma\right]}{\pi\left\{\mathrm{erfc}\left[(\psi - \psi_C)/\sigma\right)\right]^{1/2}\right\}^2} \tag{6}$$

where

$$G(\beta, y) = \int_0^y v^2 \exp\left(-\beta v^2\right) dv.$$

This normalized temperature is independent of source temperature T_{Se}. Note that $T_2(\psi_C) = T_{C2}(1 - 2/\pi)$ at the collector.

The temperature expression in Eq. (6) is composed so that the first term equals $m\langle V_2^2\rangle/\sigma T_{Se}$ and the second term equals $m\langle V_2\rangle^2/\sigma T_{Se}$. Because σ is typically 0.01, these kinetic energy and drift energy terms may differ by a very small amount so that evaluating this expression will require an accuracy of at least 32 significant digits. Secondary electron temperature is a highly sensitive indicator of beam heating not accounted for by conservation of energy. This theoretical evaluation and results from simulation for $T_2(\psi)$ will be compared in Sec. IV.

Kinetic energy flux Q is determined next in evaluating the third velocity moment. Often, Q is normalized with FT_{Se} and referred to as the energy transmission factor or power transmission coefficient δ. Integrating $v^3 f_2(\psi, v)$ over all velocities and dividing by FT_{Se} determines δ_2 as

$$\delta_2(\psi) = -\gamma(1 - \gamma)^{-1}(\sigma + \psi - \psi_C).$$

Including the full-Maxwellian distributions in the two transverse directions in this integration gives

$$\delta_2(\psi) = -\gamma(1 - \gamma)^{-1}(2\sigma + \psi - \psi_C).$$

From derivations in the previous work and contributions from the two transverse directions in velocity, then δ can be expressed for the ions as

$$\delta_i(\psi) = 2\tau - \psi, \tag{7}$$

and for the primary electrons as

$$\delta_e(\psi) = (1-\gamma)^{-1}(2+\psi-\psi_C). \tag{8}$$

Combining these three equations gives the total energy transmission factor δ_T as

$$\delta_T(\psi) = 2\tau - \psi_C + (2-2\gamma\sigma)(1-\gamma)^{-1} \tag{9}$$

which is independent of position.

With σ typically a small number, the contribution of δ_2 to δ_T is negligible. As $\gamma \to 1$, for $\tau \leq 1$, the major contribution to δ_T is from the $2(1-\gamma)^{-1}$ term from primary electrons in Eq. (8). With the mean kinetic energy defined as Q_α/F_α, Eqs. (7) and (8) show that ions arrive at the collector with a mean kinetic energy of $T_{Se}(2\tau - \psi_C)$ and electrons arrive with a mean kinetic energy of $2T_{Se}$.

A portion of the kinetic or total energy flux is the heat flux which indicates the thermal flow of thermal energy. The heat flux H is evaluated exactly in terms of the previously derived profiles using the definition given in Eq. (8) of the earlier paper. The form of H_2 for secondary electrons is the same as that for the other species except with F replaced by $-\gamma F/(1-\gamma)$; hence,

$$H_2(\psi) = Q_2(\psi) + \frac{3\gamma}{2(1-\gamma)} F T_2(\psi) + \frac{\gamma}{2(1-\gamma)} F m \langle V_2(\psi)\rangle^2.$$

Evaluated at the collector, this expression becomes

$$\frac{H_2(\psi_C)}{F T_{Se}} = \frac{\gamma\sigma}{1-\gamma}\left(\frac{2}{\pi} - \frac{1}{2}\right).$$

For $\sigma = 0.01$ and $\gamma/(1-\gamma) \leq 19$ (to be shown later), then the heat flux carried by secondary electrons away from the collector is quite small.

D. Derivation of $\psi_C(\mu,\tau,\sigma,\gamma)$ and $\psi_P(\mu,\tau,\sigma,\gamma)$

With reference to Fig. 1, the potential is characterized by $\nabla^2\psi_P = 0$ somewhere between the source and collector sheaths. Hence setting the net charge density to zero in Poisson's equation at this inflection point ψ_P gives $N_i(\psi_P) = N_e(\psi_P) + N_2(\psi_P)$. This equation can be substituted with $N_i(\psi_P)$ and $N_e(\psi_P)$ (with F adjusted) from Eqs. (11) and (12) of the earlier paper to provide the relation between ψ_C and ψ_P as

$$\frac{1-\gamma}{\sqrt{\mu\tau}}\exp\left(\frac{-\psi_P}{\tau}\right)\operatorname{erfc}\left(\frac{-\psi_P}{\tau}\right)^{1/2} = \exp(\psi_P-\psi_C)\left[1+\operatorname{erf}(\psi_P-\psi_C)^{1/2}\right] + \frac{\gamma}{\sqrt{\sigma}}\exp\left(\frac{\psi_P-\psi_C}{\sigma}\right)\operatorname{erfc}\left(\frac{\psi_P-\psi_C}{\sigma}\right)^{1/2}. \tag{10}$$

Recall that the assumption of zero net electric current (floating collector) has been included in the solution for these densities.

A second equation relating ψ_C and ψ_P results from imposing the zero electric field condition at the inflection point ψ_P. Integrating Poisson's equation, $\nabla^2\psi = 4\pi e^2 T_{Se}^{-1}(N_e + N_2 - N_i)$, once from $\psi = 0$ to $\psi = \psi_P$ and utilizing the zero field condition at both points is equivalent to integrating Eq. (10) over the same limits. The resulting expression can be written as a sum of separate terms of the normalized integral densities $\mathcal{P}$ for ions, primary electrons, and secondary electrons which respectively are

$$\mathcal{P}_i = (1-\gamma)\sqrt{\frac{\tau}{\mu}}\left[\exp\left(\frac{-\psi_P}{\tau}\right)\operatorname{erfc}\left(\frac{-\psi_P}{\tau}\right)^{1/2} - 1 + \left(\frac{-4\psi_P}{\pi\tau}\right)^{1/2}\right],$$

$$\mathcal{P}_e = \exp(\psi_P-\psi_C)\left[1+\operatorname{erf}(\psi_P-\psi_C)^{1/2}\right] + \frac{2}{\sqrt{\pi}}(-\psi_C)^{1/2} - \frac{2}{\sqrt{\pi}}(\psi_P-\psi_C)^{1/2} - \exp(-\psi_C)\left[1+\operatorname{erf}(-\psi_C)^{1/2}\right],$$

and

$$\mathcal{P}_2 = \gamma\sqrt{\sigma}\left[\exp\left(\frac{\psi_P - \psi_C}{\sigma}\right)\operatorname{erfc}\left(\frac{\psi_P - \psi_C}{\sigma}\right)^{1/2} + \frac{2}{\sqrt{\pi}}\left(\frac{\psi_P - \psi_C}{\sigma}\right)^{1/2} - \frac{2}{\sqrt{\pi}}\left(\frac{-\psi_C}{\sigma}\right)^{1/2} - \exp\left(\frac{-\psi_C}{\sigma}\right)\operatorname{erfc}\left(\frac{-\psi_C}{\sigma}\right)^{1/2}\right].$$

Thus the zero field condition at ψ_P is that the normalized integral densities sum to zero,

$$\mathcal{P}_i + \mathcal{P}_e + \mathcal{P}_2 = 0. \tag{11}$$

Together Eqs. (10) and (11) define the source sheath drop ψ_P and collector potential ψ_C in terms of the ratios of electron/ion mass, ion/primary electron temperature, primary/secondary electron temperature, and secondary electron emission coefficient. The potential dependence of the density and integrated density for each species in the terms of Eqs. (10) and (11) is identical to that derived by McIntyre[12] (in Case 2(a)) for a monotonically decreasing potential.

At critical emission, i.e. the condition when the electric field is zero at the collector, the dependence of the critical emission coefficient γ_c on μ, τ, and σ can be derived. This condition is used to derive a third expression for ψ_C and ψ_P which is valid only when $\gamma = \gamma_c$. Again, Poisson's equation is integrated this time with limits from ψ_P to ψ_C and set equal to zero because of the zero field condition at both limits. The resulting expression can be written, again in separate terms, for the normalized integral densities $\mathcal{C}$ for ions, primary electrons, and secondary electrons which respectively are

$$\mathcal{C}_i = (1-\gamma)\sqrt{\frac{\tau}{\mu}}\left[\exp\left(\frac{-\psi_P}{\tau}\right)\operatorname{erfc}\left(\frac{-\psi_P}{\tau}\right)^{1/2} - \exp\left(\frac{-\psi_C}{\tau}\right)\operatorname{erfc}\left(\frac{-\psi_C}{\tau}\right)^{1/2} - \left(\frac{-4\psi_C}{\pi\tau}\right)^{1/2} + \left(\frac{-4\psi_P}{\pi\tau}\right)^{1/2}\right],$$

$$C_e = \exp(\psi_P - \psi_C)\left[1 + \mathrm{erf}(\psi_P - \psi_C)^{1/2}\right] - 1 - \frac{2}{\sqrt{\pi}}(\psi_P - \psi_C)^{1/2},$$

and

$$C_2 = \gamma\sqrt{\sigma}\left[\exp\left(\frac{\psi_P - \psi_C}{\sigma}\right)\mathrm{erfc}\left(\frac{\psi_P - \psi_C}{\sigma}\right)^{1/2} - 1 + \frac{2}{\sqrt{\pi}}\left(\frac{\psi_P - \psi_C}{\sigma}\right)^{1/2}\right.$$

Thus the zero field condition at ψ_C is also that the normalized integral densities sum to zero,

$$C_i + C_e + C_2 = 0. \tag{12}$$

At critical emission, simultaneous solution of Eqs. (10), (11), and (12) determines ψ_C, ψ_P, and γ_c with a particular μ, τ, and σ. One solves for γ_c by varying γ until all three curves, which relate ψ_C and ψ_P for each equation, intersect at the same point. In Fig. 2, a typical curve is plotted from each equation for a D-T plasma ($\mu = 1/4590$) with $\tau = 1$ and $\sigma = 0.01$. For these parameters, γ_c is found to be is 0.899 which determines that $\psi_C = -0.99$ and $\psi_P = -0.39$. (An accuracy of three decimal places is needed for γ_c to express ψ_C and ψ_P to two decimal places.) Figure 2 represents a typical set of curves for all parameters evaluated.

E. Evaluation of potential dip

When a surface material has a coefficient of secondary electron emission beyond γ_c for the applicable plasma parameters, then the electric field reverses sign and a potential minimum occurs just in front of the collector. The secondary electrons encounter a decelerating potential from ϕ_C to ϕ_M (see Fig. 1). In the region between x_M (at ϕ_M) and $x = L$, the velocity distribution of the secondary electrons is a cut-off, decelerated Maxwellian. Consequently the maximum value of V_{M2} can be expressed through conservation of energy as

$$V_{M2}(x) = \left[\frac{2}{m}(e\phi(x) - e\phi_M)\right]^{1/2}. \tag{13}$$

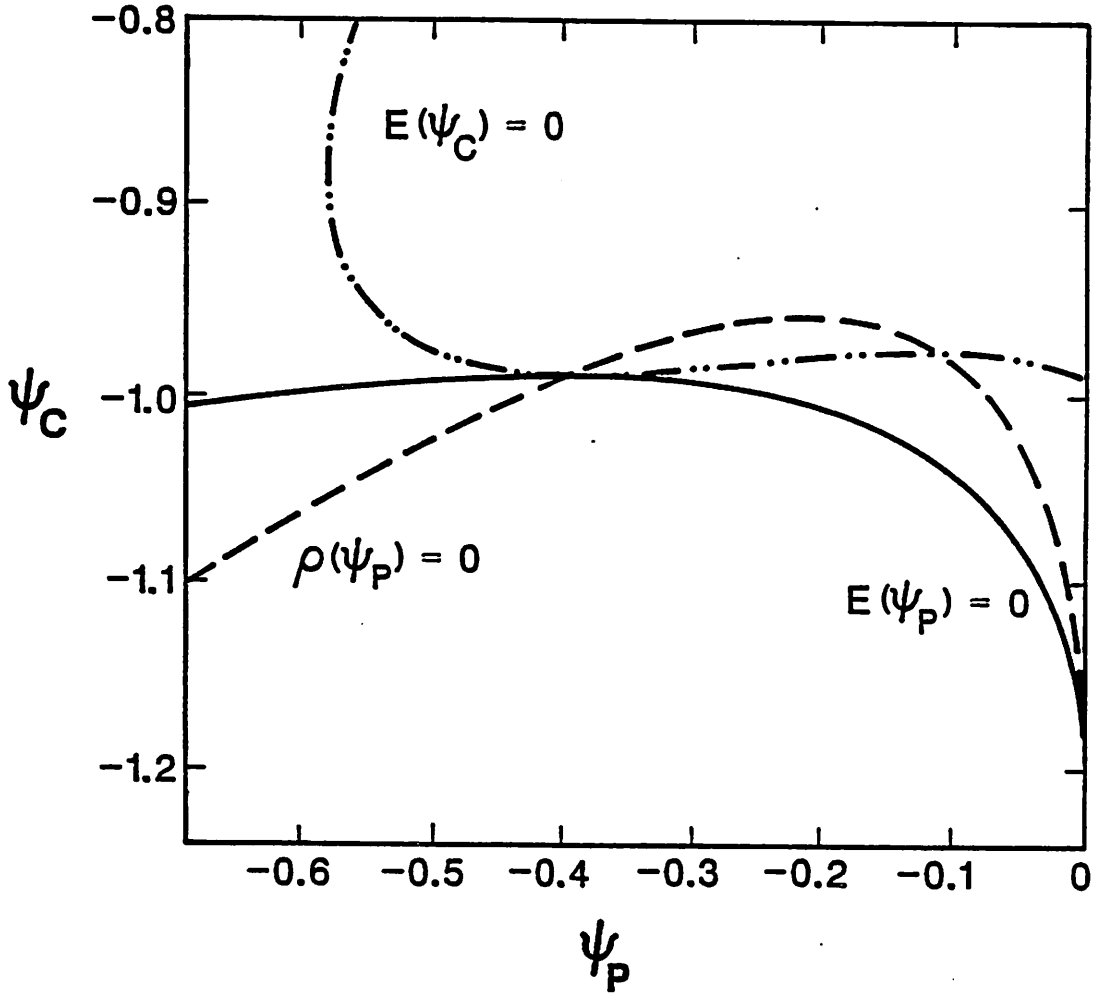

FIG. 2. Solutions of ψ_C vs. ψ_P at critical emission γ_c with the neutral charge density ρ expression at ψ_P in Eq. (10), the zero field E condition at $\psi = \psi_P$ and $\psi = 0$ in Eq. (11), and the zero field condition at ψ_C in Eq.(12) for a D-T plasma with $T_{Si}/T_{Se} = 1$ at the source. The value of γ_c is 0.899. The potentials are normalized as $\psi = e\phi/T_{Se}$.

The velocity distribution of these secondary electrons, f_2, for any potential value is the same as that given in Eq. (1) (with the above value for V_{M2}).

For $\gamma > \gamma_c$, the potential dip allows only the secondary current, emitted when $\gamma = \gamma_c$, to pass into $x < x_M$, beyond the collector sheath. As a result, the flux F_2, assumed equal to $-\gamma_c F_e$, is constant for all ψ by flux conservation, and can be written as

$$\gamma_c F_e = N_{C2}\left(\frac{m}{2\pi\sigma T_{Se}}\right)^{1/2} \exp\left(\frac{-\Delta\psi}{\sigma}\right), \tag{14}$$

where $\Delta\psi = \psi_C - \psi_M$. The flux emitted at the collector is calculated as the integral of vf_2, over all negative velocities, and is set equal to $-\gamma F_e$. This integral over the emitted distribution gives

$$\gamma F_e = N_{C2}\left(\frac{m}{2\pi\sigma T_{Se}}\right)^{1/2} \tag{15}$$

and is valid only at $x = L$. Substituting Eq. (15) into Eq. (14) defines the potential dip as

$$\Delta\psi = \sigma \ln(\gamma/\gamma_c). \tag{16}$$

(The observation of this potential dip in simulation will be discussed in Sec. III.) Hall and Bernstein [8] have derived the same expression for $\Delta\psi$. For emission well beyond space charge saturation, the potential dip $\Delta\psi$ equals approximately σ. Hence, for $\sigma = 0.01$, then $\psi_C \approx \psi_M$. By this reasoning, the technique used in Sec. II D to solve for values of ψ_C and ψ_P is valid for $\gamma > \gamma_c$ whenever $\psi_C \approx \psi_M$.

F. Analytical results

1. *Potential drops across the collector and source sheaths*

A family of curves for γ_c, which combine the solutions of Eqs. (10), (11), and (12), as a function of mass ratio for three temperature ratios, $\tau = 0.1$, 1, and 10 with $\sigma = 0.01$ is shown in Fig. 3. (Hereafter, the secondary electron temperature ratio $\sigma = 0.01$ is used for all analytical results.) The maximum value of γ_c is 0.933 for $\mu = 10^{-4}$ and $\tau = 0.1$. From this result, the maximum current of secondary electrons allowed beyond the collector sheath is $\gamma_c/(1-\gamma_c)F = 13.9\,F$. For large mass ratios, the plotted curves of $\gamma_c(\mu)$ for $\tau = 1$ and $\tau = 0.1$ are nearly the same; whereas, for $\tau = 10$, the curve is significantly lower.

The curves in Fig. 4(a) indicate $\psi_C(\mu,\tau)$ and $\psi_P(\mu,\tau)$ at critical emission and are generated simultaneously with the corresponding curves of $\gamma_c(\mu,\tau)$ in Fig. 3. For materials with emission coefficients of $\gamma > \gamma_c$, these curves represent the minimum magnitudes of ψ_C and ψ_P allowed. Maximum magnitudes of $\psi_C(\mu,\tau)$ and $\psi_P(\mu,\tau)$ occur for no secondary electron emission ($\gamma = 0$) and are shown in Fig. 3(a) of the previous work. Observe in Fig. 4(a) that the potential drop through the source sheath, ψ_P, changes significantly with source temperature ratio τ. As τ is decreased, ψ_P contributes increasingly to the total potential drop from the plasma source to the collector, ψ_C.

The curves in Fig. 4(b) indicate $\psi_C(\mu,\tau) - \psi_P(\mu,\tau)$ at critical emission and are derived from Fig. 4(a). Although ψ_P is strongly dependent on τ (in Fig. 4(a)), the potential drop through the collector sheath, changes little with τ (in Fig. 4(b)). For example, with large mass ratio, $\psi_C - \psi_P$ is nearly the same for $\tau = 0.1$ as for $\tau = 1$. Observe the curious trend that the curve of $|\psi_C - \psi_P|$ for $\tau = 1$ falls between the curves for $\tau = 0.1$ and $\tau = 10$. Cooler ions (relative to electrons) allow a greater γ_c, as shown in Fig. 3, but also increase $|\psi_C - \psi_P|$, as deduced from Fig. 3(a) of the

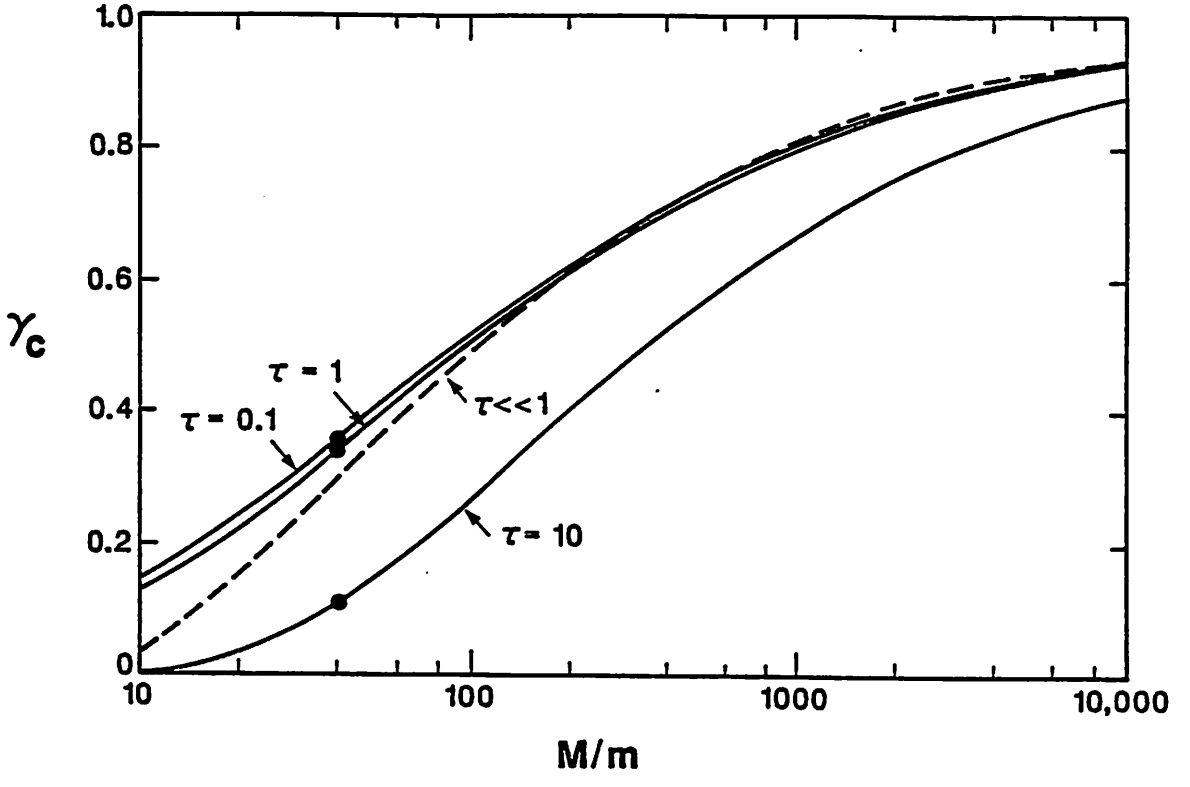

FIG. 3. Critical emission γ_c *vs.* mass ratio, $1/\mu$, from kinetic theory for three source temperature ratios $\tau = T_{Si}/T_{Se}$ (solid curves), from Hobbs and Wesson (dashed curve) for cold ions $\tau \ll 1$, and from simulation at $M/m = 40$ for three values of τ (circles).

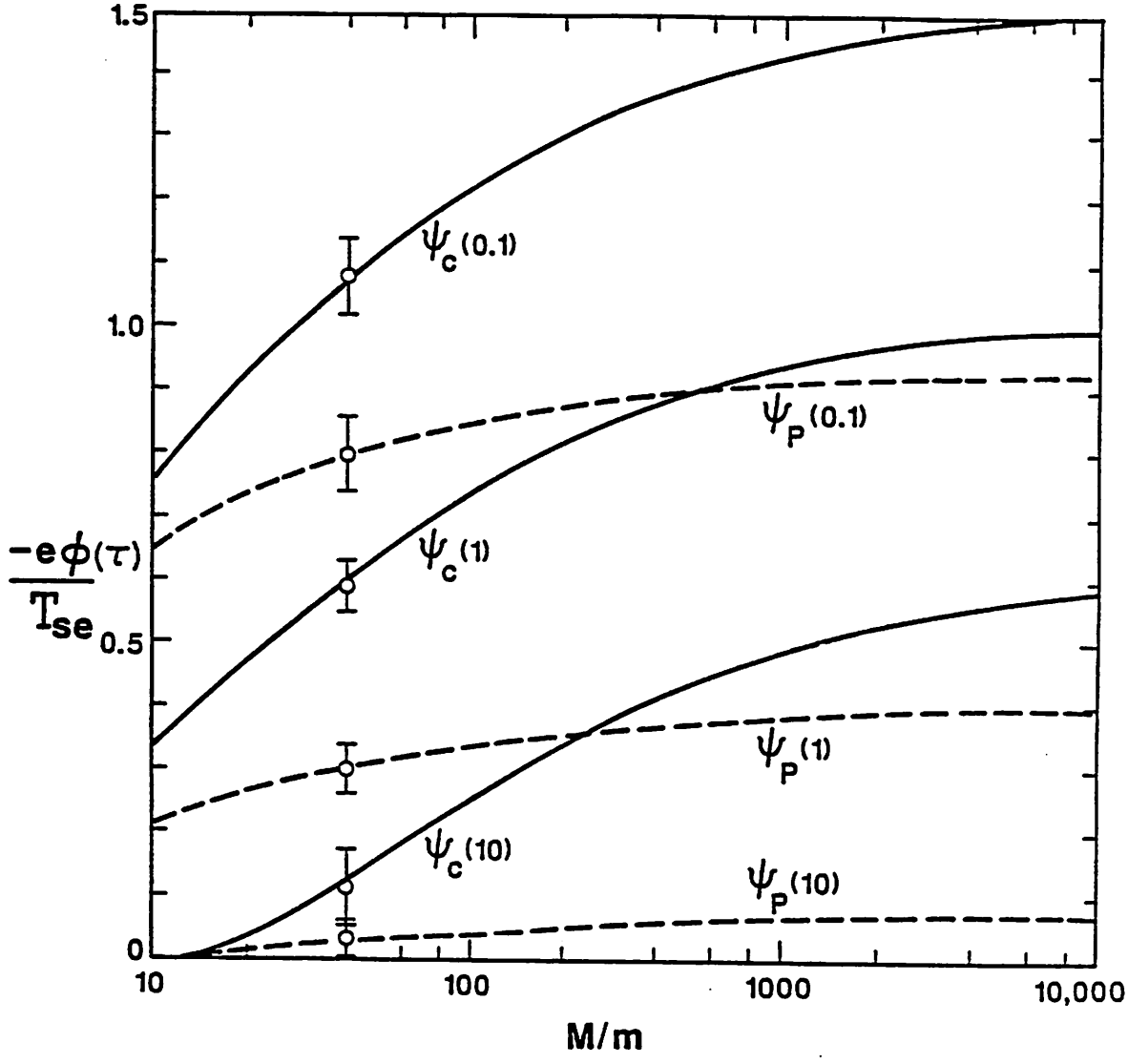

FIG. 4(a). Potentials at critical emission γ_c at two locations as a function of mass ratio, $1/\mu$. Collector potential ψ_C (solid curves) and source sheath potential drop ψ_P (dashed curves) are from kinetic theory for three source temperature ratios $\tau = T_{Si}/T_{Se}$. Open circles indicate ψ_P and ψ_C from simulation for $M/m = 40$ with $\gamma > \gamma_c$; bars indicate oscillation amplitudes at each ψ_C and ψ_P. The potentials are normalized as $\psi = e\phi/T_{Se}$.

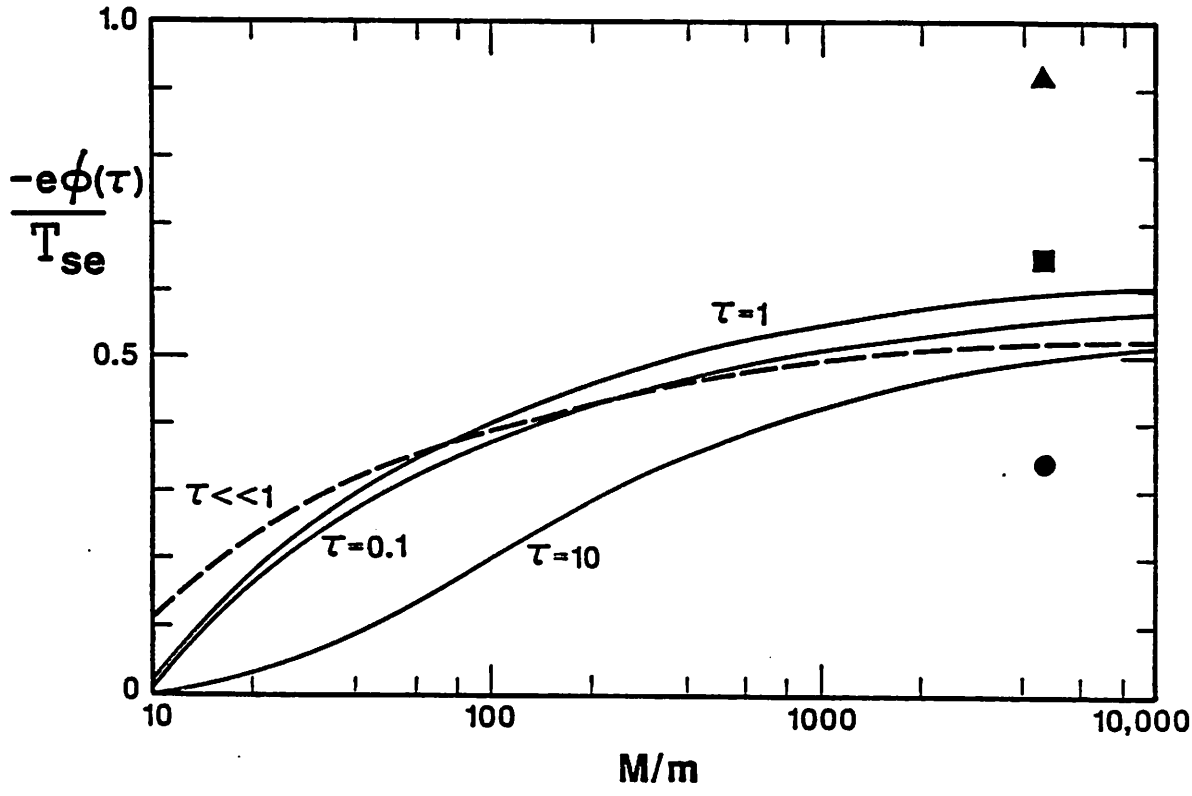

FIG. 4(b). Potential drop across the collector sheath as a function of mass ratio, $1/\mu$. Kinetic theory results (solid curves) of $\psi_C - \psi_P$ for three source temperature ratios $\tau = T_{Si}/T_{Se}$ are from Fig. 4(a). Collector sheath potential drop ψ_F (dashed curve) is from Hobbs and Wesson for cold ions, $\tau \ll 1$. Solid data points for a D-T plasma indicate Stangeby's solution for ψ_F at γ_c for $\tau = 0.1$ (triangle), $\tau = 1$ (square), and $\tau = 10$ (circle). The potentials are normalized as $\psi = e\phi/T_{Se}$.

previous paper.[3] Hence, plotting this collector sheath drop at critical emission for each τ causes a competing effect between a higher γ for the lower τ which results in the curious relative position of the curves in Fig. 4(b). With this argument, then increasing γ by only a few percent has a stronger effect on potential than decreasing τ by a factor of ten for $\tau \leq 1$.

The overall effect of γ on ψ_C and ψ_P at a particular μ for three temperature ratios is displayed in Fig. 5. Equations (10) and (11) are solved for ψ_C and ψ_P at $\mu = 1/40$ with $\tau = 0.1$, 1, and 10 for a wide range of emission coefficients. (The low mass ratio of 40 is chosen to compare with simulation results in the next section.) For $\gamma > \gamma_c$, $\psi_C(\tau)$ and $\psi_P(\tau)$ become abruptly independent of γ. Beyond critical emission, solutions for $\psi_C(\tau)$ and $\psi_P(\tau)$ are identical to those indicated in Fig. 4(a) for $\mu = 1/40$.

The sharp kink in the behavior of $\psi_C(\gamma)$ and $\psi_P(\gamma)$ in Fig. 5 is consistent with the general behavior indicating the formation of a potential barrier. Kuhn[12] also observes this kink behavior as the potential profile changes from monotonically decreasing to single-maximum and from monotonically increasing to single-minimum. Abrupt transitions appear in the dependence of central potential, density, and effective temperature on the neutralization parameter α as are shown in Fig. 2(a) and 2(b) of his paper.

Using a collector surface with increased emission (for $\gamma < \gamma_c$) decreases the magnitude of the collector potential, while slightly increasing $|\psi_P|$. In particular for $\mu = 10^{-4}$ and $\tau = 1$, $-\psi_C(\gamma)$ decreases from $-\psi_C(0) = 3.70$ to $-\psi_C(\gamma_c = 0.930) = 1.01$ and $-\psi_P(\gamma)$ increases from $-\psi_P(0) = 0.34$ to $-\psi_P(\gamma_c = 0.930) = 0.40$. McIntyre[13] also observes a similar trend in the analysis of the thermionic convertor with anodic emission. For the monotonically decreasing potential profile, reducing the cold

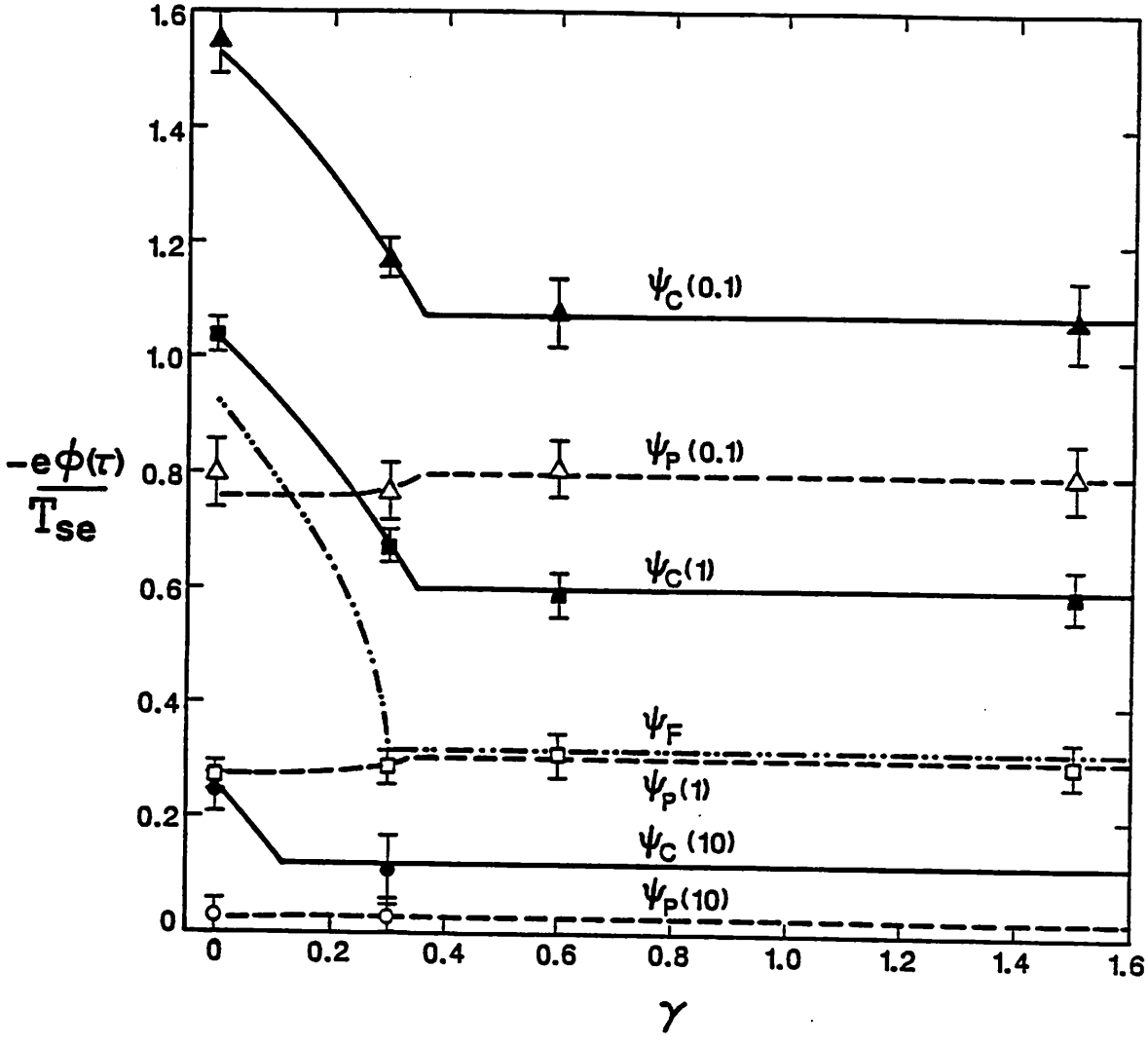

FIG. 5. Potentials at various locations for $M/m = 40$ as a function of secondary electron emission coefficient γ. Collector potential ψ_C (solid curves) and source sheath potential drop ψ_P (dashed curves) are from kinetic theory for three source temperature ratios $\tau = T_{Si}/T_{Se}$. Collector sheath potential drop ψ_F (dot-dashed curve) for cold ions $\tau \ll 1$ is from Hobbs and Wesson. Data points indicate simulation values for ψ_C (solid) and ψ_P (open) at $\tau = 0.1$ (triangles), $\tau = 1$ (squares), and $\tau = 10$ (circles); bars indicate oscillation amplitudes at each ψ_C and ψ_P. The potentials are normalized as $\psi = e\phi/T_{Se}$.

anode bias for a constant neutralization parameter causes a rise in central potential, as seen in Fig. 3(d) of his paper.

2. *Energy transport to the collector*

Using the above values of $\psi_C(\mu,\tau,\gamma)$, the effect of secondary emission on the total energy transport coefficient $\delta_T(\mu,\tau,\gamma)$ is calculated with Eq. (9) for $\psi=\psi_C$ and is displayed in Fig. 6. The shaded areas indicate, for each $\tau=0.1$, 1, and 10, the range of $\delta_T(\mu,\tau)$ generated by varying γ from 0 to $\gamma_c(\mu,\tau)$ at each mass ratio. (For $\gamma>\gamma_c$, $\delta_T(\mu,\tau)$ equals that ocurring when $\gamma=\gamma_c$.) This figure shows the large increase in energy transported from the plasma to the collector as γ is increased from 0 to γ_c. The effect of γ on δ_T becomes stronger at higher mass ratios. In particular, for $\mu=10^{-4}$ and $\tau=1$, $\delta_T(\gamma)$ is increased four-fold from $\delta_T(0)=7.1$ to $\delta_T(\gamma_c)=29.1$.

The overall effect of γ on $\delta_T(\tau,\gamma)$ at a particular μ for three temperature ratios is displayed in Fig. 7. Equation (9) for $\psi=\psi_C$ is solved for δ_T at $\mu=1/40$ with $\tau=0.1$, 1, and 10 for a wide range of emission coefficients. Energy transport coefficients δ_T are normalized to δ_T at $\gamma=0$ to show directly that increasing γ increases the total energy transported to the collector. This dependence is strongest for cooler ions. When $\tau=10$, increasing γ has little effect on δ_T because the dominant contribution to δ_T is from the ion thermal energy.

The dependence on γ of the ion contribution to the energy transported to the collector is displayed in Fig. 8. The same method used to produce Fig. 7 is employed here. Equation (7) with $\psi=\psi_C$ determines the ion energy transport coefficient $\delta_i(\gamma)$ at $\mu=1/40$ with $\tau=0.1$, 1, and 10. Values are normalized to δ_i at $\gamma=0$. In addition, these curves indicate that increasing γ reduces the mean kinetic energy of ions hitting the collector (which equals $T_{Se}\delta_i(\psi_C)$). In particular, for $\mu=10^{-4}$ and $\tau=1$, $\delta_i(\gamma_c)/\delta_i(0)$ equals 0.53 with $\delta_i(0)=3.70$. Thus a strongly emitting surface

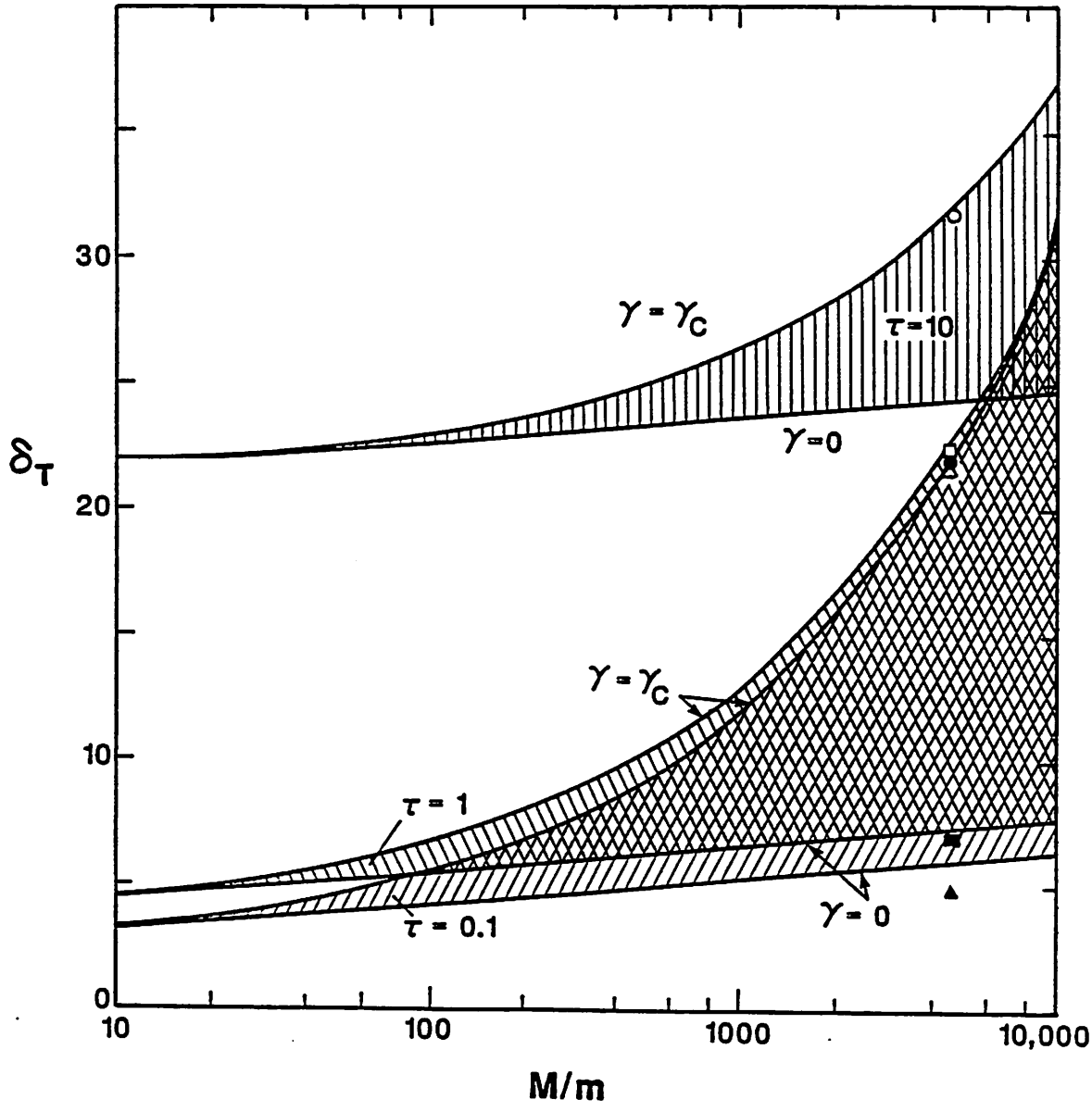

FIG. 6. Total energy transport coefficient δ_T at zero emission $\gamma = 0$ and at critical emission $\gamma = \gamma_c$ for three source temperature ratios $\tau = T_{Si}/T_{Se}$ as a function of mass ratio, $1/\mu$. The region containing the solution of δ_T, with γ is varied from 0 to γ_c, is shaded for each τ. Data points for a D-T plasma are from Stangeby with $\gamma = 0$ (solid symbols) and with $\gamma = \gamma_c$ (open symbols) at $\tau = 0.1$ (triangles), $\tau = 1$ (squares), and $\tau = 10$ (circles). Analysis assumes Maxwellian velocities in the two directions transverse to x.

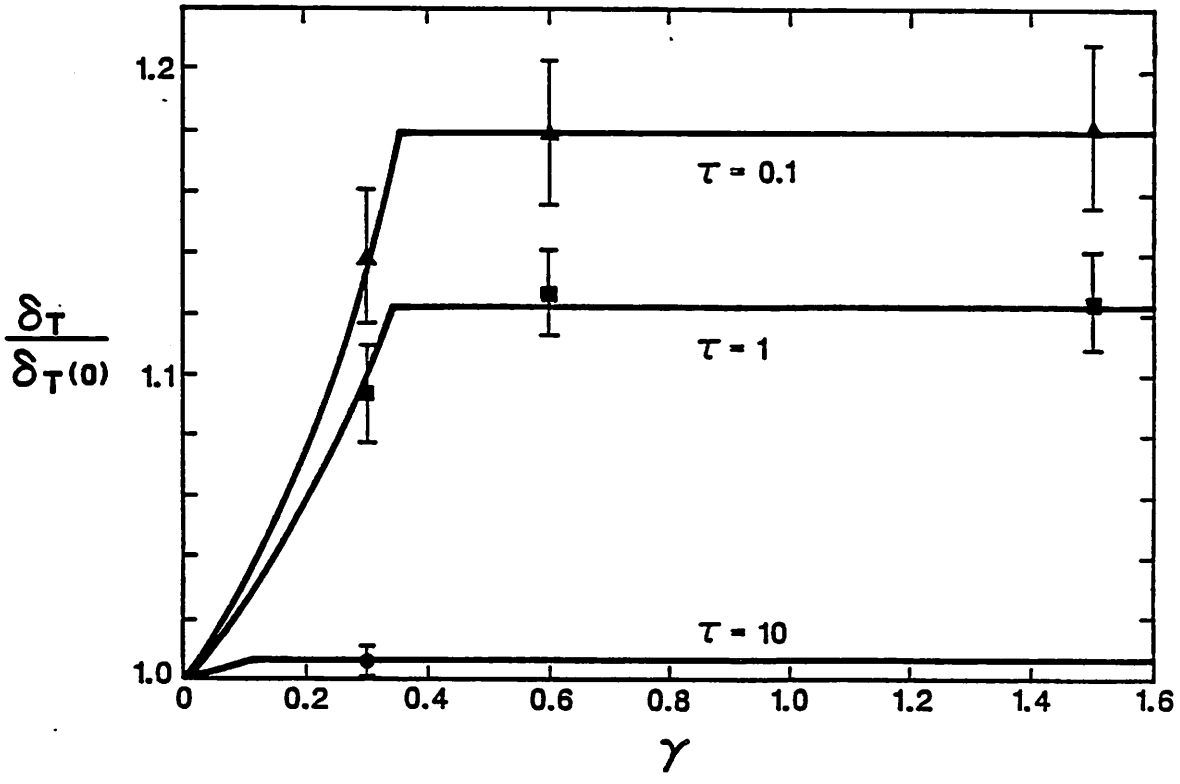

FIG. 7. Total energy transport coefficient δ_T as a function of the secondary electron emission coefficient γ at $M/m = 40$ with three source temperature ratios $\tau = T_{Si}/T_{Se}$. Solid curves indicate the kinetic theory results. Data points indicate simulation values for $\tau = 0.1$ (triangles), $\tau = 1$ (squares), and $\tau = 10$ (circle); bars indicate oscillation amplitudes of δ_T. Values of δ_T are normalized to δ_T at $\gamma = 0$. Analysis assumes Maxwellian velocities in the two directions transverse to x.

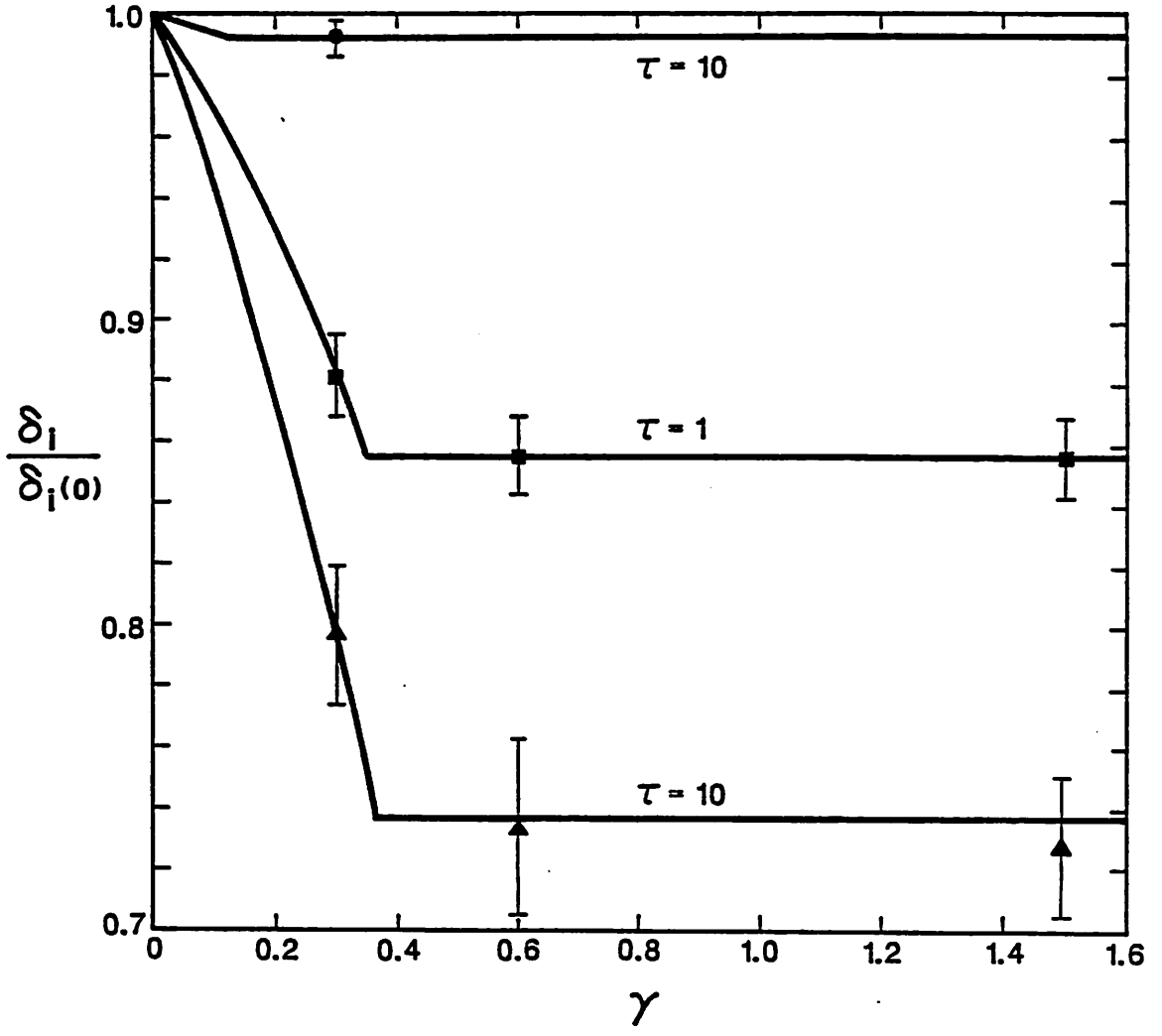

FIG. 8. Ion energy transport coefficient δ_i as a function of the secondary electron emission coefficient γ at $M/m=40$ with three source temperature ratios $\tau=T_{Si}/T_{Se}$. Solid curves indicate the kinetic theory results. Data points indicate simulation values for $\tau = 0.1$ (triangles), $\tau = 1$ (squares), and $\tau = 10$ (circle); bars indicate oscillation amplitudes of δ_i. Values of δ_i are normalized to δ_i at $\gamma=0$.

can substantially reduce incident ion energy which will reduce the sputtering rate of surface material back into the plasma.

Compared with a purely absorbing surface, an emitting collector surface creates an additional particle flux of cold electrons, which reduces $|\psi_C|$ to maintain the current balance and lower substantially the mean kinetic energy of ions reaching the surface. However, hot electrons replace the cold, emitted electrons at the collecting surface and so the energy flux of hot electrons from the plasma increases.

III. SIMULATION

A. Simulation description and fixed parameters

A particle-in-cell computer simulation for ions and electrons is used to study the region between a Maxwellian plasma source and an absorbing collector which emits electron-induced secondary electrons. Lorentz forces move the particles via electric fields derived self-consistently on a fixed mesh with Poisson's equation solved for each time step. Particles are linearly weighted to each grid where the velocity distributions are evaluated. Methods used are described in Birdsall and Langdon's book.[14] The code used here is fundamentally PDW1 composed by Lawson,[15] with surface effects and transport evaluation added.

The simulation region of $0 \leq x \leq L$, shown in Fig. 1, is initially empty. Particle electrons and ions with a mass ratio M/m of 40 are injected with equal and temporally constant fluxes. Both species enter the region at $x = 0$ with a half-Maxwellian velocity distribution with ion/primary electron temperature ratios τ of 0.1, 1, or 10. Particle secondary electrons are emitted at $x = L$ with a half-Maxwellian velocity distribution and a secondary/primary electron temperature ratio σ of 0.01. Maximum velocity values injected at the source or collector are six times the thermal velocity. The particles which return to the source at $x = 0$ are re-inserted

as injected particles with a velocity characteristic of the source temperature. No charge accumulation is allowed at the source plane; hence, the electric field at $x=0$ remains zero. At $x = L$, incident and emitted particles charge and discharge the electrically floating collector.

B. Variable parameters

Time histories and spatial profiles are presented for electrostatic potential and field, velocity scatter, temperature, and energy transport. Results are concentrated primarily on the secondary electron effects. Because $\sigma \ll 1$ is assumed, the theory for and profiles of density, drift velocity, temperature, kinetic energy flux, and heat flux for ions and primary electrons, which are presented in Figs. 5(a)–5(h) in the previous paper, indicate the same potential dependence as do the profiles for the secondary electron problem here.

All profiles except for potential are time-averaged over one plasma period from the last simulation time step after steady state is attained. Potential is not time-averaged but is a snapshot at the last time step. Steady state occurs when the average number of particles in the system becomes approximately constant with time. Time steps are typically $0.05/\omega_P$, where ω_P is the spatially averaged plasma frequency.

The systems studied are 22 Debye lengths (λ_D) long and are resolved with 6 to 50 grid cells per λ_D. This plasma Debye length is based on the steady state, length-averaged value of electron density $\overline{N}_e$. For $\gamma > \gamma_c$, a large number of grids is necessary to resolve the Debye length of the cool, high density electron cloud near the collector. A density of at least 400 particle electrons in $1\lambda_D$ is required for reduction of noise to an acceptable level; this keeps potential fluctuations below $\pm 10\%$.

C. Results for $M/m=40$ and $\tau=1$

1. *Transient behavior of collector potential and electric field*

The temporal behavior of the collector potential ψ_C and electric field E_C for $\gamma=1.5$ with $\mu=1/40$ and $\tau=1$ is displayed with the history plots shown in Fig. 9. Potential is shown normalized with e/T_{Se} and field is normalized with $e\lambda_D/T_{Se}$ (where $\lambda_D=L/22$). Typically ψ_C fluctuates with frequency ω_P which depends on $\overline{N}_e$. For reference, the calculated value of ten plasma periods is indicated next to the potential curve by the double arrow.

In Fig. 9, the collector potential begins at zero and then dips to 7.5 times the final, averaged value of ψ_C. The most negative value of ψ_C occurs when the faster electrons (with a velocity of 1.7 V_{te}) reach the collector, where $V_{te}=(T_{Se}/m)^{1/2}$. From the beginning, the collector field E_C is always negative which indicates a positive net charge at $x=L$. (For my system orientation with the collector to the right of the plasma, $E_C>0$ when $\gamma=0$.) The field becomes less negative briefly (near the time of $1\,L/V_{te}$) as incoming ions begin to neutralize the large initial negative charge at the collector. The simulation algorithm for particle injection somewhat affects this early history. In this particular simulation, because only a few particles are injected per time step, a time of approximately $3L/V_{te}$ (1500 time steps) is required before the actual time-averaged γ of 1.5 is achieved.

In reference to the simulation history of Fig. 9, potential and field reach their equilibrium value in 3.2 transit times of an ion traveling with velocity $V_{ti}((2/\pi)+(-2\psi_C/\tau))^{1/2}$ where $V_{ti}=(\tau T_{Se}/M)^{1/2}$; this time equals $15\,L/V_{te}$. By this time of potential equilibration, the ion and electron fluxes are spatially equal; however, the fluxes themselves are not yet constant in space. The fluxes become spatially constant in approximately 20 times $L(-\psi_C)^{-1/2}V_{te}^{-1}$. At this same time, by conservation of

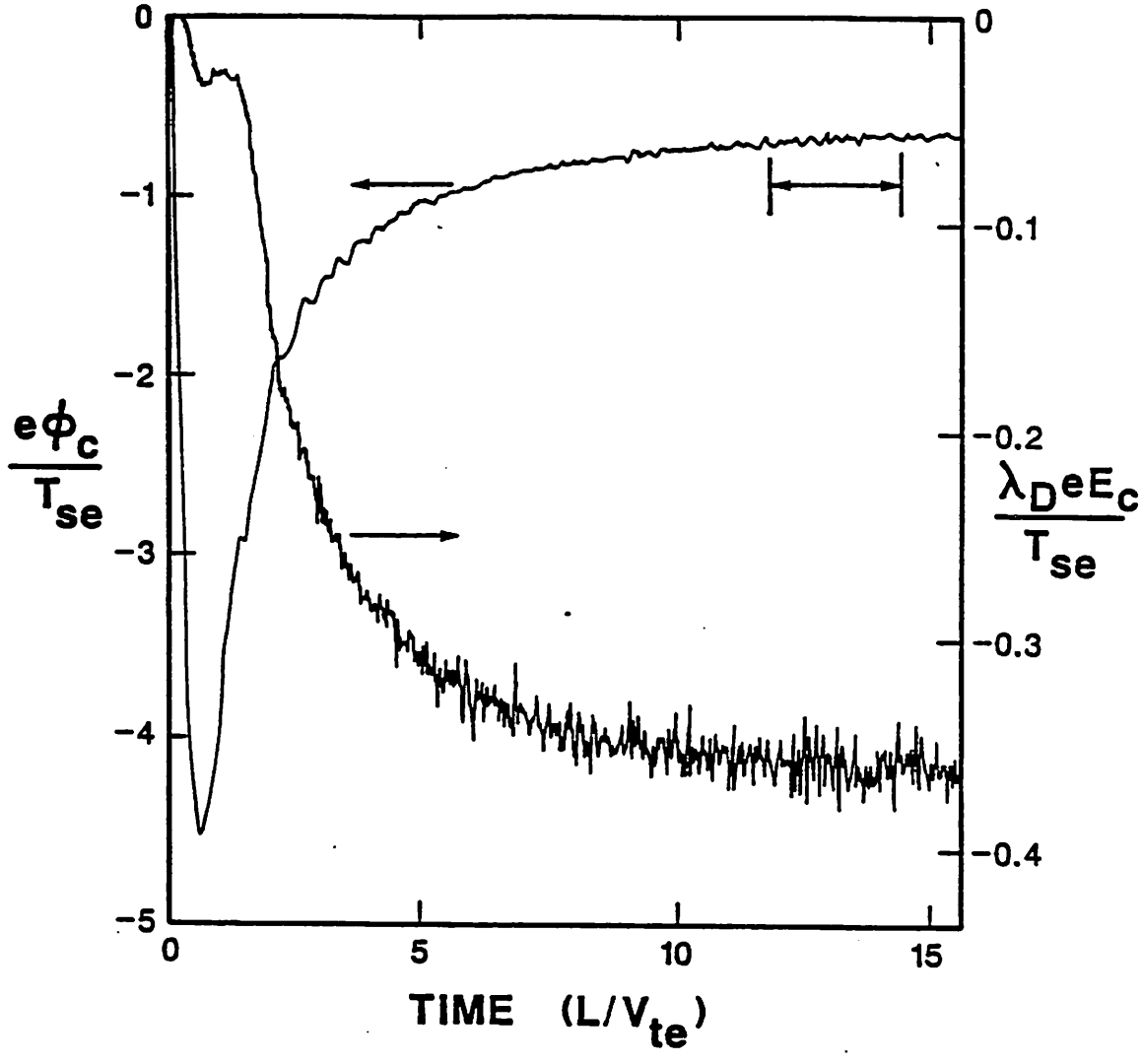

FIG. 9. History of collector potential and electric field at the collector from simulation for $\gamma = 1.5$, $M/m = 40$, $T_{Si}/T_{Se} = 1$, and $T_{C2}/T_{Se} = 0.01$. The system length L is $22\,\lambda_D$. Arrows indicate the calculated value of ten plasma periods determined from the length-averaged (total) electron density. Normalized potential $e\phi_C/T_{Se}$ and normalized field $eE_C\lambda_D/T_{Se}$ are measured at $x = L$.

particles, the total number of system particles becomes temporally constant. All plots shown hereafter are calculated at a time after particle equilibration.

The final values of ψ_C and E_C are very close to those predicted theoretically. For the above simulation parameters of $\mu = 1/40$ and $\tau = 1$ with $\gamma > \gamma_c$, the predicted value of ψ_C from Fig. 5 is -0.60. The steady state value of ψ_C seen in Fig. 9 is -0.59 with potential fluctuations of ± 0.05. For $\gamma > \gamma_c$, Sizonenko[9] estimates the magnitude of the collector field E_C as

$$E_C = T_{Se}(e\lambda_D)^{-1}(E_0/T_{Se})^{1/4}$$

where E_0 is the upper energy of emitted secondaries. If E_0 is assumed to be approximately $2\sigma T_{Se}$ then the normalized field, $eE_C\lambda_D/T_{Se}$, equals 0.38. This calculated value of normalized E_C is roughly that measured at steady state in Fig. 9.

2. *Spatial profiles at steady state*

a. Electrostatic potential. The electrostatic potential profiles shown in Fig. 10 are generated via particle simulation for $\gamma = 0.3$ and $\gamma = 1.5$ using $\mu = 1/40$, $\tau = 1$, and a length of $22\lambda_D$. The large ripples observed have a wavelength of approximately $5\lambda_D$ and may be an indication of a beam-plasma interaction (discussed later). Only ripples with a maximum wavelength of approximately $1\lambda_D$ are seen in simulations with a purely absorbing collector.[3] The insert in Fig. 10 details the collector sheath region and shows that a potential dip occurs only for $\gamma = 1.5$. With the higher γ can be observed a slightly increased magnitude of ψ_P (at $x = L/2$) and a slightly decreased magnitude of ψ_C. These trends are predicted in Fig. 5.

The magnitude and location of the potential dip compares well with earlier predictions. With these plasma parameters, the theoretical value of γ_c from Eqs. (10), (11), and (12) is 0.345. For $\gamma = 1.5$, this value of γ_c, and $\sigma = 0.01$, then $\Delta\psi = 0.015$. The potential dip from the simulation snapshot, shown in the insert of

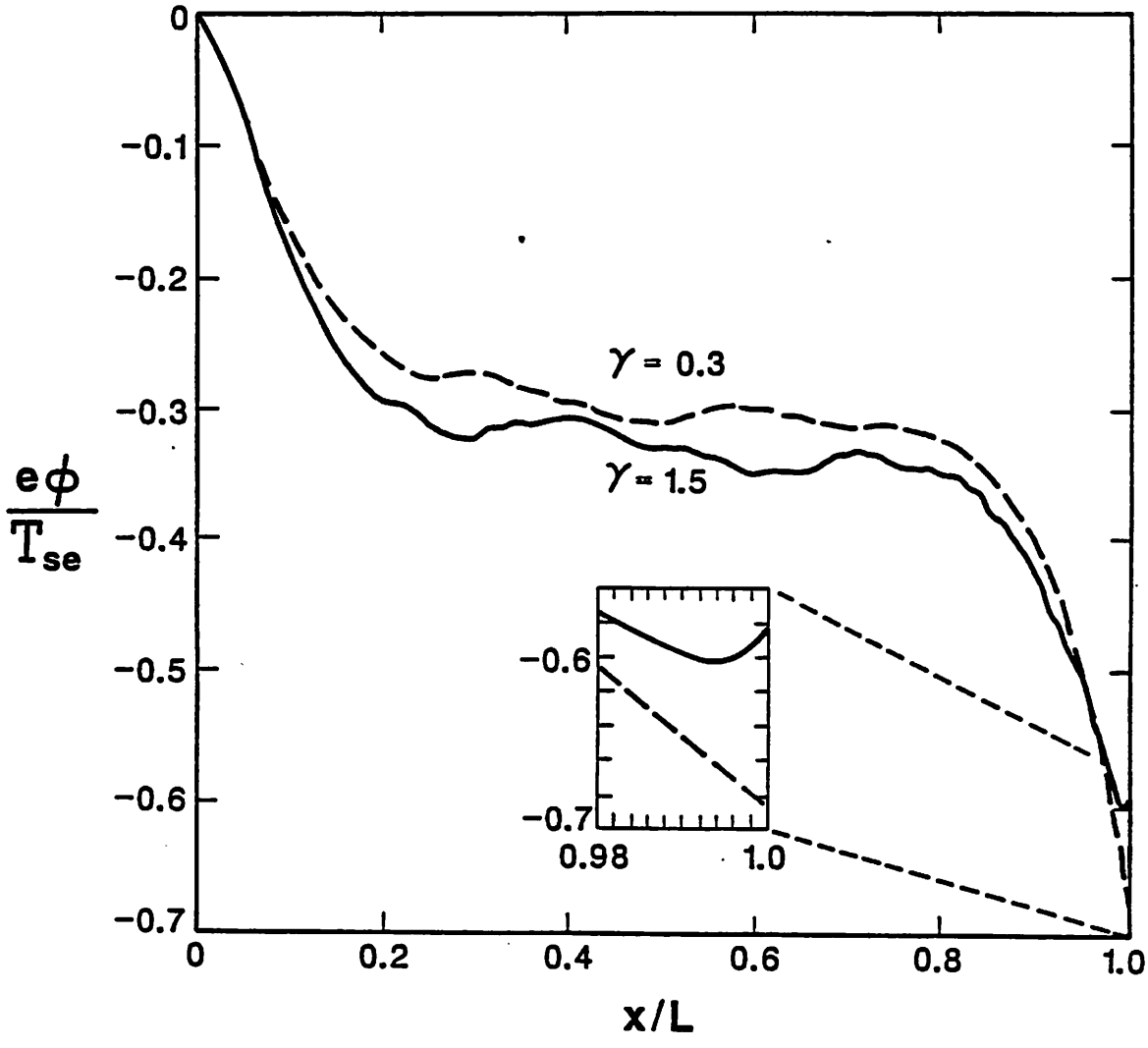

FIG. 10. Potential profiles from simulation for 2 secondary electron emission coefficients γ with $M/m = 40$ and $T_{Si}/T_{Se} = 1$. The insert details the region about $0.2\lambda_D$ from the collector. The system length L is about $22\lambda_D$. Critical emission for $M/m = 40$ and $\tau = 1$ is 0.345. The potentials are normalized as $\psi = e\phi/T_{Se}$.

Fig. 10, has a depth of $\Delta\psi = 0.017$ and so compares well to theory. The location of the potential minimum at x_M has been estimated by Sizonenko[9] to be a distance of $\lambda_D(E_O/T_{Se})^{3/4}$ from the collector surface. Using the simulation parameters given above, the predicted value of x_M/L equals 0.998. The minimum potential from simulation occurs at $x_M/L = 0.994$. This distance from $x = L$ is within a factor of two of that estimated by Sizonenko. In this simulation over 1024 grid cells are used across the simulation length; hence, one cell width here is approximately 2 Debye lengths measured in the secondary electron cloud which formed the dip. It was found that a coarser grid produces no potential dip and also significantly overpredicts $|\psi_C|$.

b. Velocity distributions. The velocity scatter of primary and secondary electrons and ions along x, for the same simulation parameters as above, is shown in Figs. 11 and 12. Also included in these figures are the velocity distribution functions $f(x, v)$ for all three species spatially averaged from $x/L = 0.25$ to 0.75. The number of particles at each discrete value of velocity, i.e. $f(v)$, is evaluated from the velocity scatter at each gridpoint. At each discrete value of x, $f(v)$ is weighted and summed over all velocities for each species to provide the various profiles such as temperature and energy flux.

The observed behavior of the electrons and ions is predictable from the potential profile in Fig. 10. Only the fastest electrons reach the collector; the remaining slower electrons are repelled by the source and collector potential drops. A distinct cut-off electron velocity $V_{Me}(x)$ exists. The secondary electrons are accelerated by the potential and follow closely $V_{Me}(x)$. Over the simulation length of $22\lambda_D$, the secondary electrons remain beam-like and do not appear in Fig. 11 to have warmed appreciably. The ions are accelerated throughout the region and all reach the collector.

The effective emission coefficient γ_e is derived in the simulation with f_e and f_2

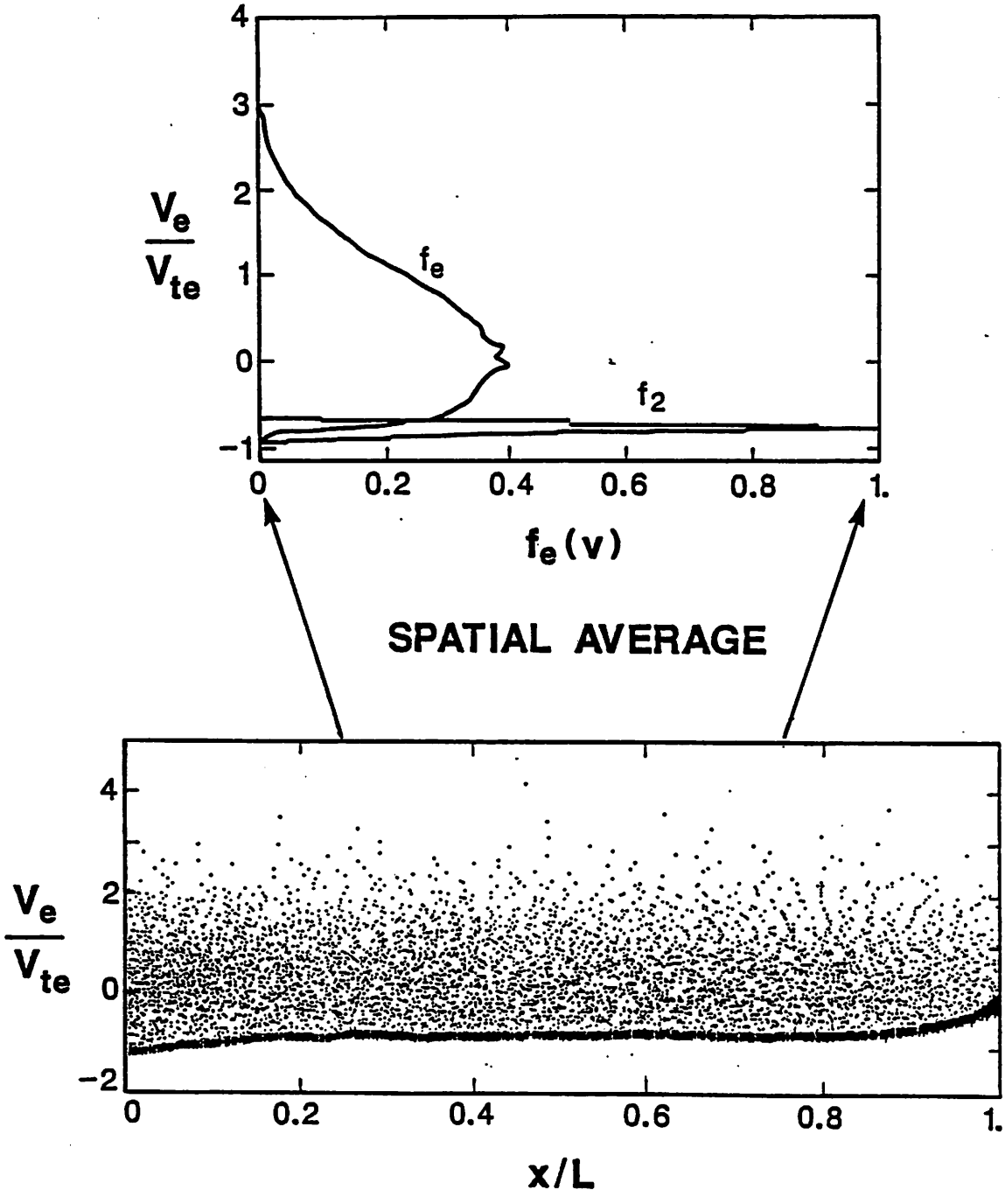

FIG. 11. Electron velocity scatter *vs.* distance and primary and secondary electron velocity distributions, f_e and f_2, averaged over the indicated spatial length. Both generated via simulation with $\gamma = 1.5$, $M/m = 40$, and $T_{Si}/T_{Se} = 1$. Electron velocities are normalized to the electron thermal velocity V_{te} at the source.

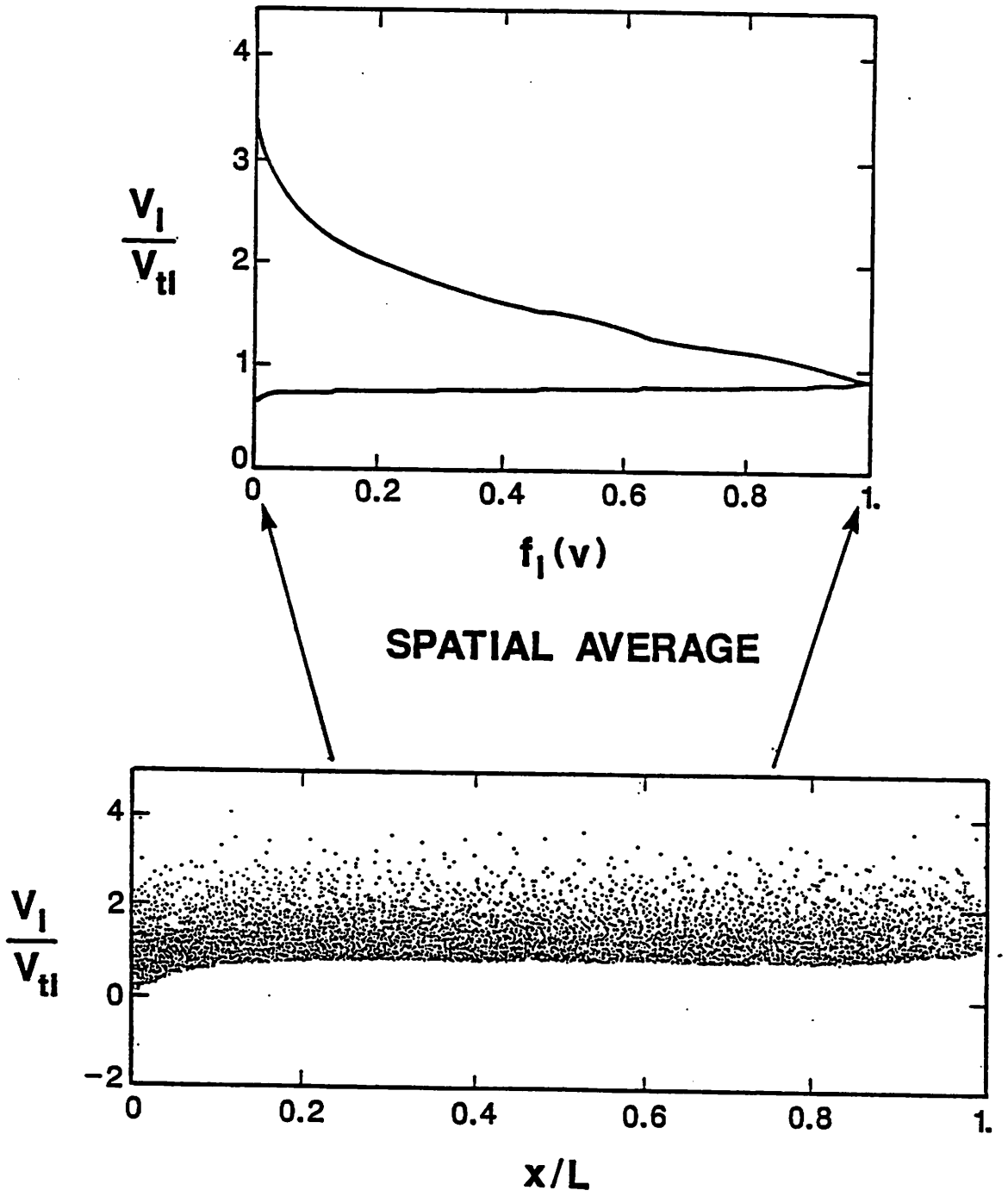

FIG. 12. Ion velocity scatter *vs.* distance and ion velocity distribution averaged over the indicated spatial length. Both generated via simulation with $\gamma = 1.5$, $M/m = 40$, and $T_{Si}/T_{Se} = 1$. Ion velocities are normalized to the ion thermal velocity V_{ti} at the source.

in Fig. 11. Effective emission is defined as the ratio of secondary electron current beyond ψ_M to the primary electron current reaching the collector. By definition, for $\gamma < \gamma_c$ then $\gamma_e = \gamma$ and for $\gamma \geq \gamma_c$ then $\gamma_e = \gamma_c$. By flux conservation, the secondary current beyond the potential dip is the same as that near $x/L = 0.5$; hence, the ratio of the fluxes (the integral over all velocities of vf_e and vf_2), measured from Fig. 11, gives $\gamma_e = 0.35$. This agrees with the value of $\gamma_c = 0.345$ calculated earlier for $\mu = 1/40$ and $\tau = 1$.

The relative magnitudes of the maximum values of $f_2(v)$ and $f_e(v)$ measured in Fig. 11 are compared with the theory derived in Sec. II. This calculation depends on ψ_C, ψ_M, γ_e, and an estimate over the region averaged of the change in $\psi(x)$, of the thermal spread in secondary electron velocities, and of the variation in cut-off velocity V_{M2}. Figure 10 indicates that $\psi_M = -0.60$ and $\psi_C = -0.583$. Over the region from $x/L = 0.25$ to 0.75, the potential varies from $\psi = -0.3$ to -0.35, again in Fig. 10. This potential change provides a range for the cut-off velocity of the secondary electrons (from Eq. (13)) of $V_{M2}/V_{te} = -0.77$ to -0.71. By energy conservation, the maximum value of $f_2(v)$ at $x = L/2$ is the same as the value of $f_2(\psi_M, 0)$. Substituting Eqs. (3) and (4) with $\gamma = 0.35$ into Eq. (1) determines that $f_2(\psi_M, 0) = 10\, F V_{te}^{-2}$. For the primary electrons, the maximum value of f_e occurs at $v = 0$; hence, substituting Eq. (2) with $\gamma = 0.35$ and Eq. (10) into Eq. (2), both from the previous paper, determines that $f_e((\psi = -0.325), 0) = 2\, F V_{te}^{-2}$. Consequently, this predicted height ratio of 5 is twice that observed in Fig. 11.

The spread in the cut-off velocity of the secondary electrons over the distance used to average f_2 accounts for the shortened spike. The thermal spread $V_{T2}(\psi)$ in f_2 is evaluated with the temperature expression in Eq. (6) and is defined as $(T_2(\psi)/m)^{1/2}$. At $\psi = -0.35$, then $V_{T2}(\psi)$, evaluated with $T_{C2}(\psi)$, equals $0.014\, V_{te}$. From the above paragraph, the average value of V_{M2} equals $0.74\, V_{te}$ with a spread

of $\pm 0.03\, V_{te}$. This spread, which is twice the thermal spread, widens the spatially averaged f_2 and reduces its magnitude by two. Hence, the above result does not yield an indication of secondary electron heating caused by a beam-plasma interaction.

c. Secondary electron temperature. A comparison of theoretical and simulation results for the effective temperature profile of the secondary electrons, $T_2(x)$, is a sensitive indicator of any thermal spreading of the beam not accounted for by energy conservation from potential variations. These profiles of $T_2(x)$ normalized to their temperature in the collector, T_{C2}, are compared in Fig. 13. Secondary electron temperature $T_2(x)$ decreases away from the collector because the increasing potential (as $x \rightarrow 0$) accelerates and thus cools (reduces the velocity spread about the mean) the velocity distribution. The simulation results for the same parameters used in Figs. 11 and 12 are plotted as a solid line in Fig. 13. The dashed line indicating theoretical results is generated by substituting the potential profile in Fig. 10 for $\gamma = 1.5$ into the expression for $T_2(\psi)$ in Eq. (6). The theoretical profile is plotted only for $x < x_M$ because Eq. (6) is valid only for a monotonically decreasing profile. The agreement between theory and simulation is good in the collector sheath. However, as $x \rightarrow 0$, the simulation profile shows evidence of heating of the secondary electron beam because of an increasing deviation from the theory curve predicted using energy conservation. Secondary electron temperature increases by a factor of five over approximately $10\, \lambda_D$. With a system length much longer than that chosen here, greater evidence of the beam-plasma interaction may be present through the increased spreading of the electron velocity distributions near V_{Me} and the increased potential fluctuations. Evidence of this beam-plasma interaction is also observed by Nicholai and Fuchs,[2] although they claim the "double-humped electron distribution is destroyed over several 10's to 100's of λ_D."

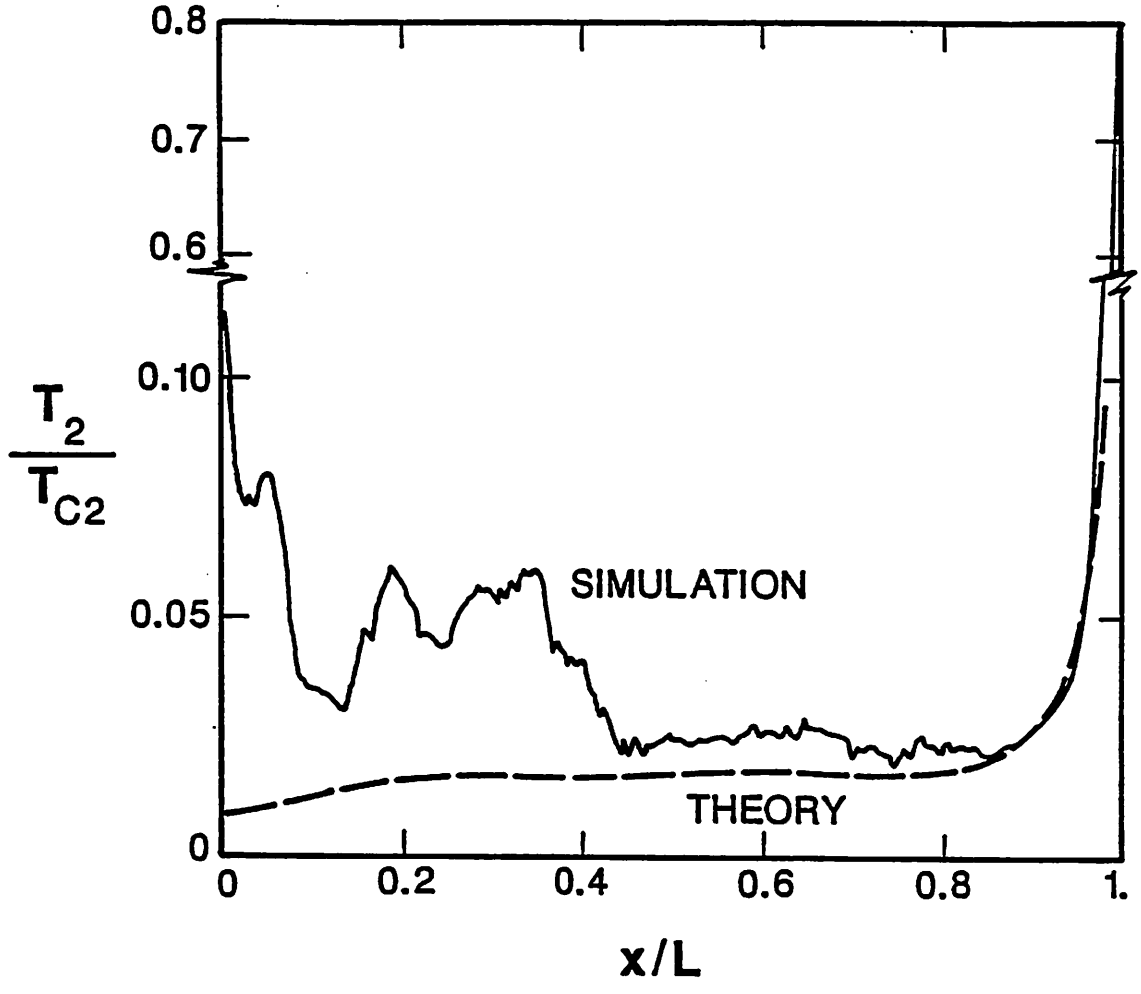

FIG. 13. Secondary electron temperature profile at $\gamma=1.5$, $M/m=40$, $T_{Si}/T_{Se}=1$, and $T_{C2}/T_{Se}=0.01$. Solid line indicates simulation results. Dashed line indicates theory from Eq. (6) determined with $\psi(x)$ from simulation in Fig. 10. Theory results are provided only for $x<x_M$, the location of minimum potential.

D. Simulation results with various γ and τ at steady state

1. *Critical emission coefficient*

With the electron source temperature fixed, raising the ion source temperature lowers the emission coefficient required to cause electric field reversal at the collector. This trend is illustrated with three simulations using $\mu = 1/40$ with $\tau = 0.1$, 1, and 10. The coefficient of critical emission is assumed to be equivalent to the effective emission γ_e as measured with the technique described in Sec. III C 2 b. The coefficient γ_e equals γ_c when $\gamma \geq \gamma_c$ which applies to simulations using $\gamma = 0.6$ and 1.5 both for $\tau = 0.1$ and 1 and using $\gamma = 0.3$ for $\tau = 10$. Each value of γ_e from these simulation measurements lies on the line of $\gamma_c(\mu, \tau)$ predicted theoretically, as plotted in Fig. 3.

2. *Collector and source sheath potentials*

The simulation values of the collector potential ψ_C and source sheath potential drop ψ_P with emission beyond collector field reversal, $\gamma > \gamma_c$ as above, agree with theory. These results for $\mu = 1/40$ are plotted in Fig. 4(a) and fall on the curves for $\psi_C(\mu, \tau)$ and $\psi_P(\mu, \tau)$. The potentials measured at $x/L = 0.5$ and 1 from Fig. 10 are those plotted respectively as ψ_P and ψ_C. The bars around each data point indicate the oscillation amplitude for each measurement of ψ_C and ψ_P. The variation of ψ_C and ψ_P over a wide range of γ also compares well with theory as detailed in Fig. 5. As predicted, for simulations with a surface that emits $\gamma = \gamma_c$ the potential profile becomes independent of γ. The difference between the potential minimum ψ_M and ψ_C is much less than the fluctuations indicated in this figure.

3. *Total energy transport*

The kinetic energy flux at the collector, $Q(\psi_C)$, is evaluated using the velocity distribution of the number of particles passing $x = L$ in each time step. This velocity

distribution of current, $vf(v)$, multiplied by v^2 yields $v^3 f(v)$ which is then integrated over all incident velocities to find $Q(\psi_C)$. To compare with theory, the simulation results in one-dimension (1-d) are adjusted to three-dimensions (3-d). The two transverse directions in velocity space are assumed to have full-Maxwellian velocity distributions. Each dimension contributes $T_{S\alpha}F_\alpha$ to Q_α, where α represents each species. Therefore, $\tau T_{Se}F$ is added to the simulation result for Q_i and $T_{Se}F_e = T_{Se}F/(1-\gamma)$ is added to the result for Q_e. Hence, the normalized contribution from the transverse directions, $\tau + (2/(1-\gamma))$, is added to δ_T, the total energy transport coefficient from the 1-d simulation results. (The contribution to δ_T by secondary electrons is negligible for $\sigma \ll 0.01$.)

These simulation results, adjusted to 3-d, appear in Fig. (7) with the theory from Eq. (9) for $\mu = 1/40$ with $\tau = 0.1$, 1, and 10. When $\gamma \geq \gamma_c$, the 3-d adjustment to δ_T uses $\gamma = \gamma_e$ measured in the simulation rather than γ_c from theory. Excellent agreement is observed between the simulation and theory over a wide range of γ. The normalization factor $\delta_T(0)$ used for simulation is actually from simulation at $\gamma = 0$. The bars on each data point indicate the oscillation amplitude in δ_T which exists even after the history values are time-averaged over a plasma period.

4. *Ion energy transport*

Simulation results for ion energy transported to the collector, which also indicate the mean ion energy at the collector, is compared with theory via Eq. (7) and plotted in Fig. 8. As described above, the value of δ_i from the 1-d simulation is adjusted to 3-d with the addition of τ. In general the comparison of these results and theory indicate good agreement. For $\tau = 0.1$, the simulation data occur increasingly below the theory as γ is raised. This discrepancy is not observed for the other cases of τ.

The presence of the potential dip, which appears when γ exceeds γ_c, causes this difference between theory and simulation for $\tau = 0.1$. With reference to Eq. (7), small corrections to ψ_C will change δ_i noticeably as τ decreases. For $\sigma \ll 1$, presumably the value of ψ_C predicted in the zero field condition at $x = L$ (in Eq. (12)) could be equated to ψ_M which is defined at the location of minimum ψ, i.e. zero field. The magnitude of ψ_C would then be of order σ less than the ψ_C given here in theory. Consequently, the dependence of δ_i on γ would be weak for $\gamma \geq \gamma_c$ with $\tau = 0.1$. This correction would lower the curves of $\tau = 0.1$ by approximately σ which for low mass ratio is noticeable. However, the other two curves for warmer ions would be negligibly affected. The contribution of δ_i to δ_T is generally much less than that from the electrons, δ_e, so that the minor corrections caused by the potential dip are insignificant in evaluating δ_T.

IV. COMPARISON WITH PREVIOUS RESULTS

A. Summary

Results of potential drop across the collector sheath, $\psi_C - \psi_P$, and the coefficient of secondary electron emission at charge saturation, γ_c, from the current work compare best with those from Hobbs and Wesson of the authors listed in Table I. General comparisons can be made for the works of Hobbs and Wesson,[5] Stangeby,[6] and Sizonenko.[9] The remaining authors in Table I do not derive an analytic expression that can be readily solved as a function of mass and temperature ratios. Consequently the work of these authors can be compared at only one set of parameters which typically is for a D-T plasma.

In the previous analyses, ions are assigned a minimum energy prior to entering the collector sheath. These authors evaluate the "floating collector potential" ψ_F, which is just the collector sheath potential drop and not the collector potential

ψ_C. My analysis determines self-consistently the potential drop through the source sheath, ψ_P, so that we can only compare $\psi_C - \psi_P$ derived here with ψ_F. This comparison assumes that the source sheath serves as a "presheath" which accelerates the ions in order to form the monotonically decreasing potential profile.

The following table summarizes results from the present analysis for a D-T plasma ($\mu = 1/4590$) which will be used as a benchmark for comparing with the results of others.

Table II. Collector potential ψ_C and potential drop across the collector sheath, $\psi_C - \psi_P$, at critical emission with coefficient γ_c at various temperature ratios, $\tau = T_{Si}/T_{Se}$, for a D-T plasma ($M/m = 4590$) derived with Eqs. (10), (11), and (12).

τ	ψ_C	$\psi_C - \psi_P$	γ_c
0.1	−1.48	−0.56	0.903
1	−0.99	−0.59	0.899
10	−0.57	−0.49	0.825

B. Simple analytic expressions

1. *Cold ions* $\tau \ll 1$

The results of Hobbs and Wesson[5] for cold ions, cold secondaries, and Boltzmann primary electrons are compared with present results using their expressions for the relation between the collector sheath drop ψ_F and the minimum ion energy entering the collector sheath, E_M. I solve Eqs. (2) and (3) of their paper simultaneously to generate plots of ψ_F versus E_M for given values of μ and γ. For each γ chosen, which is less than γ_c, two points of intersection occur; the value of ψ_F at the intersection point nearest $E_M = T_{Se}/2$ (the Bohm condition[11]) is used for

the comparison. For $\gamma > \gamma_c$, the two curves of $\psi_F(E_M)$ do not intersect which indicates no solution for the assumptions made. The γ chosen which allows the two curves to intersect at only one point is the coefficient of critical emission γ_c. (Note the similarity in technique here with that of finding ψ_C versus ψ_P at γ_c as shown in Fig. 2.)

With this technique for various values of μ, the curve of γ_c versus μ for the assumptions of Hobbs and Wesson is generated and plotted as the dashed curve in Fig. 3. This dashed curve is not determined from their approximate expression, which is $\gamma_c = 1 - 8.3\mu^{1/2}$. Best only for large M/m, this approximation is 3% below γ_c derived exactly from their Eqs. (2) and (3). Our results show close agreement with their exact solutions for $M/m > 200$ and $\tau \leq 1$. For a D-T plasma with $\tau \ll 1$, they obtain a value for γ_c of 0.91. This result is within 1% of the value of γ_c in Table II for $\tau \leq 1$ and is 10% above γ_c for $\tau = 10$.

For each M/m, determining $\gamma_c(\mu)$ from the expressions of Hobbs and Wesson simultaneously specifies the collector potential drop $\psi_F(\mu)$. Figure 4(b) compares this potential drop ψ_F (dashed curve) with my results for $\psi_C - \psi_P$ as a function of mass ratio and illustrates a reasonable agreement. Specifically, for a D-T plasma with $\tau \ll 1$, they obtain a value for ψ_F of -0.52. Relative to the values of $\psi_C - \psi_P$ in Table II, we find a difference of -6% for $\tau = 0.1$, -11% for $\tau = 1$, and $+7\%$ for $\tau = 10$.

In their own approximation of Eqs. (2) and (3), Hobbs and Wesson conclude that $\psi_F = -1.02$ and minimum ion energy $E_M = 0.58 T_{Se}$ for infinitely massive ions. An exact analysis of their Eqs. (2) and (3) (described above) gives $\psi_F = -0.53$ and $E_M = 0.76$ for $M/m = 10^4$. For large mass ratio, the dashed curve in Fig. 4(b) asymptotes to $-\psi_F$ less than 0.6 which is considerably below 1.02. Consequently,

the exact values should be used from their analysis rather than the approximate values which seem to be incorrect.

In the final comparison, even with a low mass ratio of 40 and $\tau \leq 1$, the difference between $\psi_C - \psi_P$ and ψ_F is small. Their exact expression determines that $\gamma_c = 0.301$ for $\mu = 1/40$ (and $\tau \ll 1$). In Fig. 5, we see the best comparison between our theories for emission beyond charge saturation. For $\gamma \geq \gamma_c$, then ψ_F lies above $\psi_C - \psi_P$ by 13% for $\tau = 0.1$, by 6% for $\tau = 1$, but by 240% for $\tau = 10$. This large disagreement in the last case occurs because of the breakdown in the Boltzmann approximation, i.e. with large τ causing a small ψ_F, primary electrons are nearly half-Maxwellian rather than full-Maxwellian.

The total energy flux delivered to the collector is essentially the same for both cold and warm ion models. We differ in the evaluation of ion energy flux entering the sheath region. Hobbs and Wesson find that the cold ions enter with energy E_M of at least $T_{Se}/2$ and then gain energy $T_{Se}\psi_F$ through the collector sheath. My analysis assumes that ions exit the source with mean kinetic energy τ and gain energy $T_{Se}\psi_C$. Typically the mean ion energy at the plasma edge of the collector sheath, which is assumed to equal $T_{Si} + T_{Se}\psi_P$, does not equal the same value as $T_{Se}/2$. However, the major contribution to the total energy flux Q_T is from the electrons via Q_e. For large mass ratio, Q_e/Q_T exceeds 0.95 because $\gamma_c \to 1$ which makes the $2/(1-\gamma)$ term is dominant. (This term is on page 86 of their paper and is in Eq. (9) of the present paper.)

Sizonenko[9] models the secondary electron problem more thoroughly in assuming that the secondary electrons have a finite temperature and the primary electrons have a cut-off velocity distribution. (Ions are assumed cold.) The exact, complicated analytic expression for ψ_F is dependent on the energy distribution of the secondary electrons emitted (refer to Fig. 2 of that paper). For critical emission, i.e. when

$\psi_M = \psi_C$, Sizonenko approximates this expression for ψ_F as

$$\psi_F = \ln\left[\frac{1}{\sqrt{2\pi}}\frac{V_{te}}{U}(1-\gamma_c)\right]$$

where U is the cold ion drift velocity at the sheath edge. This approximation provides results for ψ_F almost twice the value of $\psi_C - \psi_P$ from Table II.

Sizonenko also determines a "Bohm criterion" for the minimum ion energy at the sheath edge which is that the maximum V_{te}/U is $(M/m)^{1/2}$. With this result and $\gamma_c(\tau)$ from Table II (because Sizonenko does not derive $\gamma_c(\mu,\tau)$), then $\psi_F \approx -1$ for $\tau \leq 1$. If the mean ion kinetic energy at ψ_P (from Eq. (7)) is used instead of the Bohm criterion then $V_{te}/U = [2\mu(2\tau - \psi_P)]^{-1/2}$. With these results and ψ_P from Table II, then ψ_F is -0.5 for $\tau = 0.1$ and -0.2 for $\tau = 1$. Thus, it appears that use of the Bohm condition causes significant overprediction of ψ_F for cool ions.

2. *Various temperature ratios*

The results of Stangeby[6] for potential drop through the collector sheath ψ_F (referred to as the floating potential) differ substantially with the results herein; whereas, the results for energy transmission to the collector surface compare well. The expression he derives for ψ_F is

$$\psi_F = 0.5 \ln\left[2\pi\mu(1+\tau)(1-\gamma)^{-2}\right].$$

To compare with this work, the $\gamma_c(\mu,\tau)$ from my results are applied to the above equation, because Stangeby does not derive $\gamma_c(\mu,\tau)$.

Our values of ψ_F and $\psi_C - \psi_P$ are compared in Fig. 4(b) for a D-T plasma for three temperature ratios. Stangeby's values differ from mine by +64% for $\tau = 0.1$, by +10% for $\tau = 1$, and by −29% for $\tau = 10$. Thus, for emission beyond critical and large mass ratio with $\tau = 1$, his simple expression is a good approximation for the

collector sheath drop (but not collector potential). For simulation parameters with $\mu=1/40$, our results differ by over 50%.

The comparison of our values for the energy transmission coefficient at the collector is shown in Fig. 6 for a D-T plasma at three temperature ratios. Stangeby expresses the total energy transmission coefficient as

$$\delta_T = 2\tau + [2/(1-\gamma)] - \psi_F.$$

Hence, the acceleration of ions to the ion acoustic speed prior to entering the collector sheath is neglected in this expression. Substituting the earlier equation for ψ_F into the above equation for δ_T generates the data points plotted in Fig. 6 for $\mu=1/4590$. The closed and open symbols indicate values of δ_T for $\gamma=0$ and $\gamma=\gamma_c$, respectively. For the purely absorbing collector, Stangeby's values of $\delta_T(\tau)$ lie below mine primarily because of the difference in treatment of the ion energy entering the collector sheath region.* (This is discussed extensively in the previous paper.[3]) At critical emission (open data points), close agreement exists because the electrons dominate δ_T in the term of $2/(1-\gamma)$ as explained earlier for Hobbs and Wesson.

C. Complicated analyses

Harbour[7] examines the interdependence of cold secondary electron emission and collector potential drop for various values of mean ion energy entering the collector sheath. In the general analysis, electrons have a truncated Maxwellian velocity distribution and ions enter with a most probable drift speed and a finite thermal spread in velocity. However, only results for zero ion temperature are presented for a D-T plasma.

The dependence of effective emission Γ_S, where $\Gamma_S = -F_2/F_e = \gamma/(1-\gamma)$, is plotted against ψ_F and energy transport coefficient δ_T is plotted against ψ_F Figs. 4 and 5 respectively of Harbour's paper. The ion energy entering is expressed

* In Stangeby's analysis, if the minimum ion energy of $T_{Se}/2$ is included in the total energy transmission then 1/2 would be added to δ_T above, which would improve agreement in Fig. 6.

through the ion energy transport coefficient δ_i which is assumed to be equivalent to $\delta_i(\psi_P)=2\tau-\psi_P$ in Eq. (7) of the present paper. Using this equation and Table II, then $\delta_i(\psi_P)$ equals 1.1 for $\tau=0.1$ and 2.4 for $\tau=1$. (With the Bohm criterion, then $\delta_i(\psi_P)\geq 0.5$.)

Fair agreement is found with Harbour's results at critical emission; the smallest difference occurs for $\tau=0.1$. With the above δ_i for space charge limited emission, then our results for $\Gamma(\psi_F)$ and $\delta_T(\psi_F)$ can be compared using Figs. 4 and 5 of Harbour's paper. At maximum emission, the curves his Fig. 4 indicate that $\gamma_c=0.89$ and $\psi_F=0.62$ for $\tau=0.1$ ($\delta_i=1.1$) and $\gamma_c=0.86$ and $\psi_F=0.53$ for $\tau=0.1$ ($\delta_i=2.4$). Critical emission coefficients are a few percent below those in Table II. Relative to $\psi_C-\psi_P$, values of ψ_F are 10% above that for $\tau=0.1$ and 10% below for $\tau=1$. Similarly curves in his Fig. 5 predict that $\delta_T=21$ for $\tau=0.1$ and $\delta_T=23$ for $\tau=0.1$ (with the same $\psi_F(\tau)$ as above). Relative to $\delta_T(\psi_C,\gamma)$ from Eq. (9) using ψ_C and γ_c from Table II, values from this Fig. 5 underpredict δ_T by 10% for $\tau=0.1$ and by 26% for $\tau=1$.

Hall and Bernstein[8] model the secondary electron problem more thoroughly in assuming the secondary electrons have a finite temperature, $T_{C2}=\sigma T_{Se}$, but the ions are still assumed cold. Ions enter the collector sheath with a specified value of minimum energy E_M expressed with a parameter $b=T_{Se}/E_M$. They find that the maximum value of b equals 2 (the Bohm criterion) for $\gamma\rightarrow\gamma_c$. Results for ψ_F versus b at various γ are plotted in their paper for a D-D plasma ($M/m=3669$) and secondary electron temperature ratio of $\sigma=0.02$. If b is assumed to be equivalent to $1/\delta_i(\psi_P)$ (from $\delta_i(\psi)$ in Eq. (7)), then $b=0.89$ for $\tau=0.1$ and 0.42 for $\tau=1$. (These values use ψ_P calculated for a D-T plasma and $\sigma=0.01$ for the secondary electrons which are nearly the same as those for a D-D plasma as seen in the ψ_P curves for $\tau=0.1$ and 1 in Fig. 4(a).) Hall and Bernstein find that the maximum

emission coefficient occurs at $\gamma_c = 0.908$ which is a few percent above my results for γ_c for $\tau \leq 1$. They also plot curves of $\psi_F(b)$ at various γ in Fig. 2 of their paper. With the values of b from above and the curve for $\gamma = 0.9$ in their Fig. 2, we find that $\psi_F \approx -0.4$ for $\tau = 0.1$ ($b = 0.94$) and no value of ψ_F for $\tau = 1$. If we choose a smaller value of γ, interpolated to approximately 0.85 for $b = 0.42$, then $\psi_F \approx -0.2$. Consequently, this analysis of Hall and Bernstein compares well at $\tau = 0.1$ with the present analysis for γ_c but underpredicts considerably the magnitude of the collector sheath potential drop calculated with the ion energies leaving the source sheath. Shown in their Fig. 6 for cold ions, total energy flux to the collector increases by over a factor of 4 for a change in γ from 0 to γ_c for ions entering the collector sheath with the maximum value of b. This increase somewhat larger than the factor of 3.7 increase seen in the present analysis for $\tau = 0.1$.

Brooks[10] uses a time-dependent kinetic, Vlasov simulation for the sheath region where electron surface effects are combined under a total emission coefficient of R_e. Surface effects include secondary electron emission induced by both incident electrons and ions and by primary electron reflection. This total coefficient is observed to saturate at $R_e = 0.9$ for a D-T plasma with a 5% impurity fraction of beryllium ions. The ratio of ion to electron kinetic energy entering the sheath region is a fixed parameter termed α. For $\alpha = 1$, Brooks finds that $\psi_F = -0.5$ at saturated emission which is comparable to values of $\psi_C - \psi_P$ in Table II.

Nicholai and Fuchs[2] develop a transport model of plasma diffusing across magnetic field lines and then flowing to a collector which emits secondary electrons. They use the plasma parameters of TEXTOR as an example and examine the effects of using various collector materials with differing secondary electron emission coefficients. Hence only general trends of our results are compared. Comparing the plasma parameters using a beryllium surface (with low γ) and a tungsten surface

(with high γ), they find with an increased γ that $|\psi_F|$ decreases and the kinetic energy flux from electrons reaching the collector increases. These same trends for collector sheath potential drop and energy transmission as a function of secondary electron emission coefficient are seen in all of the above, past and present, analyses.

V. CONCLUSIONS

The effects of electron-induced secondary electron emission on the plasma source and collector sheaths are analyzed for ion/electron mass ratios from 10 to 10^4 with ion/electron temperature ratios τ of 0.1, 1, and 10. Emission up to and beyond field reversal at the electrically floating collector is simulated for a mass ratio of 40 with these same values of τ for emitted secondary electrons having a secondary/primary electron temperature ratio of 0.01. Density, drift velocity, temperature, kinetic energy flux, and heat flux for all three species are derived at values of potential at the collector and across the source sheath. For all of the above values, excellent agreement exists between our electrostatic particle simulation and the fully kinetic model except with the secondary electron temperature.

The profile of secondary electron temperature indicates heating not explained by the time-independent, kinetic theory presumably because of the presence of a beam-plasma interaction. For a D-T plasma with $T_{Si} = T_{Se}$, increasing the secondary emission from 0 to beyond critical emission causes the collector potential to change from -3.3 to -1 and the total energy flux to the collector surface to increase by a factor of 3.1. (Preliminary simulations show that these analytic and simulation models can also be applied to the sheath region bounded by a hot surface which emits thermionic electrons; the only difference is that cold electrons are emitted with a current independent of the incident primary electron current.)

The exact analysis of Hobbs and Wesson (rather than their approximations) shows the best overall agreement with the present results in predicting potential drop across the collector sheath ($\psi_C - \psi_P$) and the total energy flux to the collector. All of the referenced authors in Table I require that the ions attain somehow a minimum energy prior to entering the collector sheath. In my analysis and simulations, this ion energy arises self-consistently from the source sheath which is affected by secondary electron emission and represents a significant portion of the total potential drop from the Maxwellian source region to the collector. We conclude, as listed in Table I, that the present model is the nearest of the referenced works to first principles in self-consistently modeling the dynamic and kinetic behavior of the electrons and ions in the non-neutral, non-Maxwellian region between a Maxwellian plasma source and a collector emitting secondary electrons.

Acknowledgments

This research was sponsored by the U. S. Department of Energy under Contract DE-FG03-86ER53220.

References

[1]R. A. Langley, J. Bohdansky, W. Eckstein, P. Mioduszewski, J. Roth, E. Taglauer, E. W. Thomas, H. Verbeek, and K. L. Wilson, *Data Compendium for Plasma Surface Interactions,* Nucl. Fusion, special issue (1984).

[2]A. Nicolai and G. Fuchs, J. Nucl. Mater., **76–77**, 556 (1978).

[3]L. A. Schwager and C. K. Birdsall, "Collector and Source Sheaths of a Finite Ion Temperature Plasma," ERL Memo M88/23, Univ. of Calif., April 13, 1988.

[4]G. A. Emmert, R. M. Wieland, A. T. Mense, and J. N. Davidson, Phys. Fluids, **23**, 803 (1980).

[5]G. D. Hobbs and J. A. Wesson, Plasma Phys., **9**, 85 (1967).

[6]P. C. Stangeby, Phys. Fluids., **27**, 682 (1984).

[7]P. J. Harbour, Report No. CLM-P535, Culham Laboratory, Abingdon, Oxfordshire, U. K. (1978).

[8]L. S. Hall and I. Bernstein, Report No. UCID-17273, Lawrence Livermore National Laboratory, Livermore, California (1976).

[9]V. L. Sizonenko, Sov. Phys. Tech. Phys., **26**, 1345 (1982).

[10]J. N. Brooks, J. Nucl. Mater., **93–94**, 437 (1980).

[11]D. Bohm, in *Characteristics of Electrical Discharges in Magnetic Fields*, edited by A. Guthrie and R. K. Wakerling (McGraw-Hill, New York, 1949).

[12]S. Kuhn, Plasma Physics, **23**, 881 (1981).

[13]R. G. McIntyre, Proc. IEEE, **51**, 760 (1963).

[14]C. K. Birdsall and A. B. Langdon, *Plasma Physics via Computer Simulation*, (McGraw-Hill, New York, 1985).

[15]W. S. Lawson, "PDW1 User's Manual", Memo No. UCB/ERL M84/37, Electronics Research Laboratory, University of California, Berkeley, California (1984).

Variable List

Symbol	Name
ϕ_P	Source sheath potential drop
ϕ_C	Collector potential
F_α	Particle flux
γ	Secondary/primary electron emission ratio
T_{C2}	Secondary electron temperature in the collector
$T_{S\alpha}$	Source temperature
τ	Ion/primary electron source temperature ratio
M	Ion mass
m	Electron mass
μ	Electron/ion mass ratio
ϕ_M	Minimum potential
$\Delta\phi$	Potential dip
σ	Secondary/primary electron temperature ratio
γ_c	Critical emission coefficient
α	Ion/primary electron emitted density ratio
L	System length
x	Spatial position
v	Velocity
$V_{M\alpha}$	Cut-off velocity

f_α Velocity distribution function . . . . . .

N_{C2} Secondary electron density in the collector . . . . . .

ψ Normalized potential . . . . . .

N_α Particle density . . . . . .

$\langle V_\alpha \rangle$ Drift velocity . . . . . .

T_α Temperature . . . . . .

Q_α Kinetic energy flux . . . . . .

H_α Heat flux . . . . . .

F Reference particle flux . . . . . .

$N_{S\alpha}$ Source density . . . . . .

δ_α Energy transmission factor . . . . . .

δ_T Total energy transmission factor . . . . . .

$V_{t\alpha}$ Source thermal velocity . . . . . .

E_C Collector electric field . . . . . .

ψ_F Normalized potential drop across the collector sheath . . . . . .

The subscript α refers to ions i, primary electrons e, or secondary electrons 2.

The above is a list of only frequently referenced variables.